ABSTRACT

Title of Thesis:	2-DIMENSIONAL ZEOLITES FOR ADSORPTIVE DESULFURIZATION
	Jingyu Fang, Master of Science, 2018
Thesis directed by:	Professor, Dr. Dongxia Liu, Department of Chemical and Biomolecular Engineering

The removal of sulfur-containing compounds from transportation fuels is of growing urgency due to the increasingly government stringent regulations. Adsorptive desulfurization at ambient conditions is a promising strategy for sulfur-containing compound removal compared to traditional hydrodesulfurization (HDS) that requires high temperature and pressure. In this thesis, we studied zeolite adsorbents for adsorptive desulfurization of model fuels. Three zeolite frameworks (MFI, MWW and FAU) in both 2-dimensional (2D) and 3D structures were synthesized and ion-exchanged to both proton-form and Ag^+-form. The adsorption of thiophene and benzothiophene, respectively, in n-octane was done using both H^+- and Ag^+-form zeolites in both 2D and 3D structures. The results show that 2D zeolites have high

adsorption capacity than 3D analogues in removal of benzothiophene. The Ag^{+}-form zeolites increase the adsorption capacity compared with that of H^{+}-form. In terms of zeolite framework effects, MWW zeolites possesses the highest adsorption capacity.

2-DIMENSIONAL ZEOLITES FOR ADSORPTIVE DESULFURIZATION

by

Jingyu Fang

Thesis submitted to the Faculty of the Graduate School of the
University of Maryland, College Park, in partial fulfillment
of the requirements for the degree of
[Master of Science]
[2018]

Advisory Committee:
Professor Dongxia Liu, Chair
Professor Chunsheng Wang
Professor Taylor J. Woehl
Dr. Dat T. Tran

Dedication

This work is dedicated to my parents and sister, Xiaofu Zhang, Yumin Fang and Jiayi Fang, who greatly supported and encouraged me during my graduate study. I will not have chance to study abroad and finish my Master's degree without them.

Acknowledgments

I want to thank my advisor, Dr. Dongxia Liu, for her patient instructions and guidance during my graduate study and research in her group. No matter when I ran into a trouble spot or had questions about my research or writing, she always diligently helped me. She always encourages and directs me to think critically, which is an important research ability for a graduate student.

Thank you Dr. Dongxia Liu, Dr. Chunsheng Wang, Dr. Taylor Woehl and Dr. Dat Tran for taking time to serve on my committee.

I would like to thank Dr. Dat Tran for his generous help in XRD and DR UV-vis characterization of my zeolites samples.

I would like to thank my labmates for their patient guidance and assistance during my one and half years stay in Dr. Liu's lab. I want to thank Su Cheun Oh for her assistance of characterization using scanning electron microscopy and the knowledge of gas chromatography. I want to thank and Wei Wu for his assistance in using scanning electron microscopy. I would like to thank Yiqing Wu and Junyan Zhang for sharing their zeolites knowledge and their help in XRD characterization. I would like to thank Mann Sakbodin for the help of making alumina pellets. I would like to thank

Dongchang Qin for sharing the knowledge about UV-vis spectroscopy. I would like to thank Emily Schulman for helping me with gas chromatography.

At last, I would like to thank my all my friends for making me stay here meaningful and memorable.

Table of Contents

List of Tables

List of Figures

Figure 4-9. Equilibrium adsorption isotherms of benzothiophene (top) and Langmuir model linear fitting (bottom) over Ag-2D MWW, Ag-3D MWW, Ag-2D FAU, Ag-3D FAU, Ag-2D MFI and Ag-3D MFI materials. (adsorbents mass: 0.015g; model fuel mass, 0.5g; adsorption temperature, 23℃; adsorption time, 12h).

Figure 4-10. Thiophene and benzothiophene adsorption over Ag^{+}-zeolites at same conditions.

Chapter 1: Introduction

1.1 Environmental and health effect

Deep reduction of sulfur in transportation fuels is of growing urgency due to the increasingly stringent government regulations in many countries worldwide. In EU countries, the acceptable level of sulfur in diesel fuel in vehicle exhaust emission was reduced from the original value of 1000 parts per million (ppm) to 10 ppm in 2014 (Table 1.1). [1] Similarly, the U.S. Environmental Protection Agency (EPA) Tier 3 program required that federal gasoline will not contain more than 10 ppm of sulfur on an annual average basis by January 1, 2017. [2]

Table1-1. Sulfur content in diesel and gasoline fuel according to the European standard requirement. [1]

Standard	The time of standard beginning to work	Sulfur content(ppm)	
		Diesel fuel	Gasoline fuel
Euro 1	1994 (October)	2000	1000
Euro 2	1999 (January)	500	500
Euro 3	2000 (January)	350	150
Euro 4	2005 (January)	50	50
Euro 5	2009 (January)	10	10
Euro 6	2014 (September)	10	10

The driving force behind the stringent regulations is related to the harmful effects of SO_2 which comes from the combustion of organosulfur -containing fuels. Short-term exposures to SO_2 can pose a threat to human respiratory and cardiovascular system. In

addition, high concentration of SO_2 contributes to the formation of particulate matter which may penetrate deeply into lungs and cause additional health problems. As for the environmental effect, SO_2 emissions can result in acid rain and harm ecosystem. [3-9]

SO_2 (g) +1/2 O_2 (g) → SO_3 (g)

SO_3 (g) +H_2O (l) → H_2SO_4 (aq)

1.2 Sulfur compounds in transportation fuels

Sulfur-containing compounds in transportation fuels can be generally classified into two groups: one is aliphatic sulfur compounds such as mercaptanes and sulfides which can be easily removed by hydrodesulfurization; the other is aromatic organosulfur compounds including thiophene and its derivatives which are more intractable than aliphatic compounds to desulfurize. Table 1-2 listed the typical sulfur compounds in transportation fuels.

Table 1-2. Major sulfur compounds in transportation fuels. [10]

Transportation fuel type	Sulfur compounds
Gasoline range, light naphtha, and FCC naphtha	Mercaptanes (RSH), Sulfides (R_2S), Disulfides (RSSR), Thiophene and alkylated-thiophenes, and Benzothiophene
Jet Fuel range, heavy naphtha, and middle distillate	Benzothiophene (BZT) and its alkylated derivatives
Diesel Fuel range, middle distillate, and light crude oil	Alkylated-benzothiophenes, Dibenzothiophene (DBT) and alkylated-dibenzothiophenes

1.3 Current desulfurization method – hydrodesulfurization

Commercially, the most mature technology for sulfur removal is hydrodesulfurization (HDS) which is carried out with Co-Mo/Al_2O_3 or Ni-Mo/Al_2O_3 catalysts. This process consumes hydrogen and requires high temperature (300-380 ℃) and high pressure (above 30 bar). [11-12] Generally, the organosulfur compounds are converted into non-sulfur organics and H_2S gas in HDS process as shown in Figure 1-1. [13] However, HDS can hardly achieve ultra-low sulfur fuels while maintaining fuel requirements because of the low reactivity of some refractory sulfur compounds such as poly-aromatic sulfur compound and substituted thiophenic compounds.

Types of Organic sulfur compounds	Mechanism of hydrotreating reaction
Mercaptanes	$R\text{-}SH + H_2 \rightarrow R\text{-}H + H_2S$
Sulfides	$R\text{-}S\text{-}R' + 2H_2 \rightarrow R\text{-}H + R'\text{-}H + H_2S$
Disulfides	$R\text{-}S\text{-}S\text{-}R' + 3H_2 \rightarrow R\text{-}H + R'\text{-}H + 2\,H_2S$

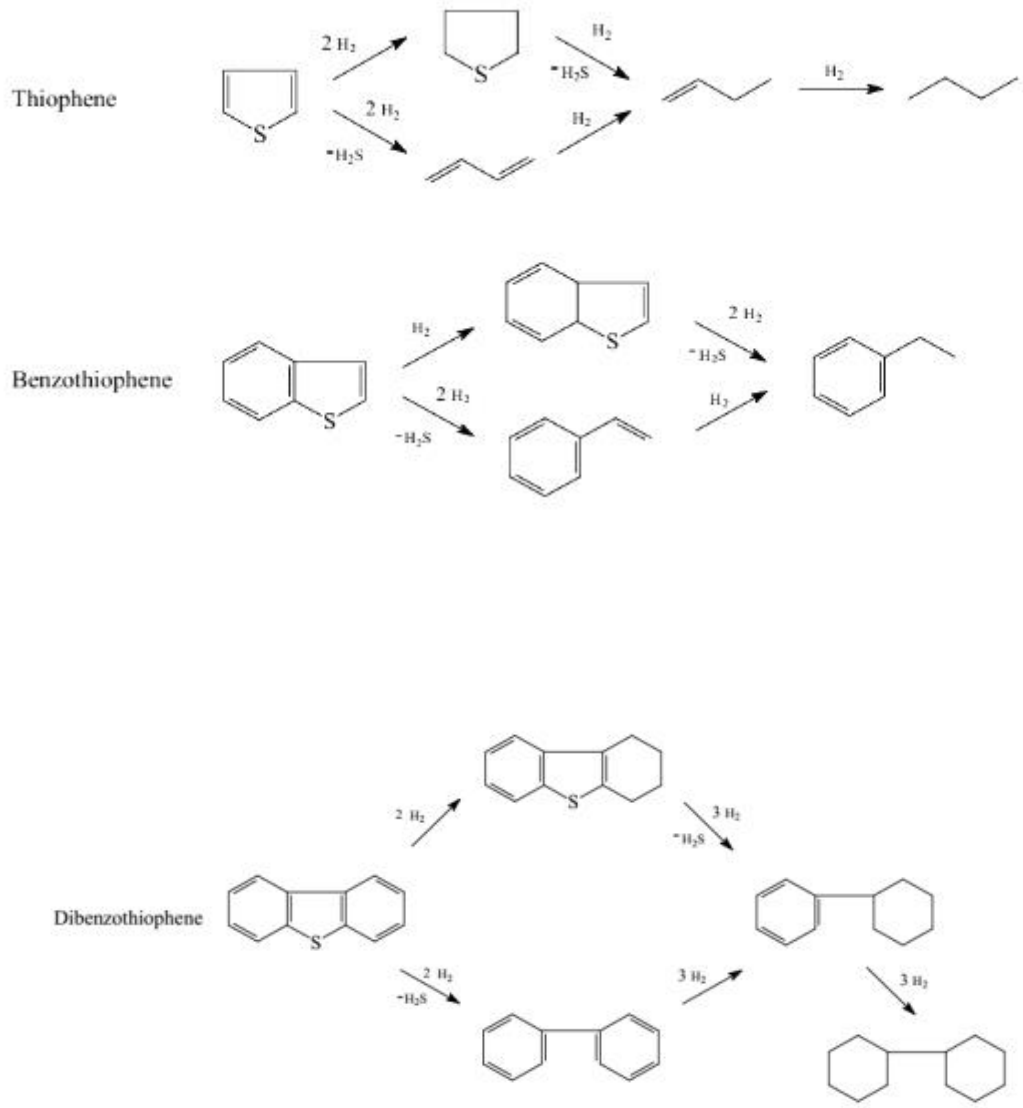

Figure 1-1. Organosulfur compounds and their hydrotreating pathways. [13]

The reactivity of sulfur containing compounds in HDS process is affected by the type and size of sulfur molecules. As shown in Figure 1.2, aliphatic sulfur compounds like thiols, mercaptanes and sulfide exhibit higher reactivity, because they do not have a conjugation structure between the lone pairs on S atom and the π electrons on aromatic ring.[14] However, for the sulfur compounds with one to three rings, the reactivity decreases in the order thiophenes > benzothiophenes > dibenzothiophenes. In addition, the more methylated sulfur compounds are much less reactive than the non- substituted ones. Overall, deep reduction of sulfur is hindered by the poly-aromatic sulfur compounds as well as the substituted sulfur compounds.

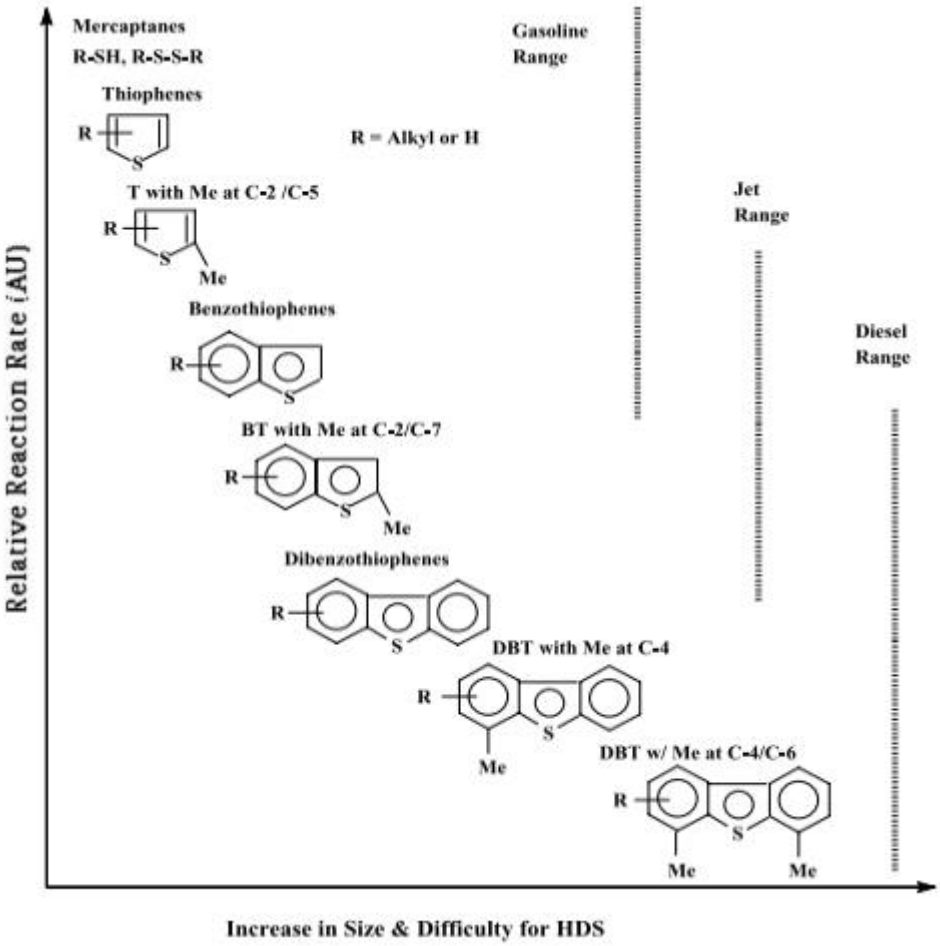

Figure 1-2. Reactivity of various organic sulfur compounds in HDS versus their ring sizes and positions of alkyl substitutions on the rings. [14]

On the other hand, conventional HDS process also results in the hydrogenation of alkenes and arenes, which lowers the octane number of gasoline and cetane number of diesel. Another drawback of conventional HDS for deep desulfurization is the high energy input due to severe reaction condition at high temperature and pressure, especially the high need for hydrogen.

1.4 Selective adsorption removal of sulfur compounds

As a consequence, development of new desulfurization methods is needed. Recently, researchers has been developing alternatives for the desulfurization of liquid fuels such as adsorptive desulfurization, using ionic liquid as extractants and bio-desulfurization. [15-17] In this respect, selective adsorption removal of sulfur (SARS) is a promising method for ultra-deep desulfurization with the help of adsorbents. Contrary to conventional HDS, SARS can be operated at low temperatures and ambient pressure without consuming hydrogen, preventing hydrogenation which usually occurs during HDS process. In addition, the milder conditions of SARS also decreases the cost of desulfurization process.

Among many adsorbents, zeolites have attracted much attention for desulfurization because of its high surface area, molecular sieve properties, acidic features of its proton form and the ion exchange ability. Most of the SARS by using zeolites focused on investigating the adsorption ability of Y zeolites because its cage-like cavity can reach up to 13Å which is able to accommodate large organosulfur compounds. Most researches were carried out with model gasoline, diesel and jet fuels

containing different organosulfur compounds like thiophene, benzothiophene, dibenzothiophene and 4,6-dimethyldibenzothiophene.

In 1990's, H^+- zeolites like H-ZSM5 and HFAU have been investigated for thiophene adsorption. Gracia [18] concluded that thiophene bonds to the SiOHAl groups on H-ZSM5 zeolites surface and undergoes ring opening reaction followed by oligomerization. Later, Richardeau [19] investigated thiophene adsorption over HFAU zeolites in a stirred batch system at room temperature and further confirmed the adsorption ability of acidic zeolites. Chica [20] studied effects of zeolite structure and alumina content on thiophene adsorption over H-ZSM5, H-Beta and H-Y with varying Si/Al ratios. They found that thiophene adsorption uptakes (per Al) do not depend on their Al content, but were above unity due to oligomerization and affected by the channel volume and the spatial constraints within zeolites channels.

Besides H^+- zeolites, researches have been carried out over zeolites exchanged with transition metals in parallel. Yang [21] reported excellent thiophene adsorption performance of Cu^{2+} and Ag^+ exchanged Y zeolites compared to NaY zeolites, mainly due to the π-complexation between the transition metals and the organosulfur compounds. The capacity for thiophene followed the order Cu-Y and Ag-Y >> Na-ZSM-5 > activated carbon >Na-Y > modified alumina and H-USY. Later on, Xue [22] investigated adsorption of thiophene in an organic model gasoline by a batch method at 80℃ using metal ion-exchanged Y zeolites. As reported, Na-Y exchanged with Ag^+, Cu^{2+}, Ce^{3+} ions showed remarkable high adsorptive capacity for thiophene and follows the order of CuY < AgY < CeY. Except for Cu^{2+}, Ag^+, Ce^{3+} ions, Song[23] investigated

Ni-based adsorbent and found that sulfur compound are adsorbed by the direct S-M bond formation using the lone pair of electrons of the sulfur atom present in the plane of the ring rather than π-complexation using delocalized electrons of the aromatic ring.

Meanwhile, more bulky organosulfur compound such as benzothiophene and dibenzothiophene has also been investigated. S. Velu [24] studied the desulfurization performance of JP-8 jet fuel containing 736 ppm of sulfur over different transition metal ion-exchanged Y-zeolites in a batch reactor at 80℃. Zeolite Y exchanged with Ce exhibits highest sulfur capacity of 2.7 mgS/g of adsorbents and the decrease in the order CeY > PdY > NiY > HY > CuY > ZnY. In a later research, Bhandari [25] reported a very high sulfur removal capacity over Ni-Y (~ 42 mg/g) and Cu-Y (~ 31 mg/g) zeolites with the trend: NiY > CuY > FeY > ZnY > NaY.

There are some inconsistencies in the ranking of the sulfur capacity over the same metal ion-exchanged Y zeolites in the works mentioned above. This suggests that the sulfur capacity is not solely affected by the chemical composition but also influenced by other factors such as the type of sulfur compounds, the method used to load metals, the selection of model fuels or commercial fuels and the experimental adsorption method.

Hernandez et al. [26] investigated desulfurization performance of Cu^{+}, Ni^{2+} or Zn^{2+} exchanged Y zeolite by using different techniques such as liquid phase ion exchange (LPIE) and solid-state ion exchange (SSIE). The performance decreases follows the order: Cu(I)-Y(VPIE) > Ni(II)-Y(SSIE) > Ni(II)-X(LPIE) > Zn(II)-X(LPIE) > Zn(II)-Y(LPIE). They pointed that the means of introducing copper ions(I)

are essential and LPIE cannot achieve completely ion exchange because the hydration state of the cupric ions and the complex hydrolysis mechanisms. Desulfurization of transportation fuels with zeolites under ambient conditions have been reported by Yang et al. Yang[27] showed Cu and Ag ion exchanged Y zeolite are capable of selectively adsorbing sulfur compounds from commercial fuels at ambient temperature and pressure. And the sulfur content can be reduced from 430 to <0.2 parts per million by weight (ppmw) at a sorbent capacity of 34 cubic centimeters of clean diesel produced per gram of sorbent.

1.5 Mechanism of sulfur removal

1.5.1 π- complexation

Based on the π- complexation, cations can form a σ-bond with their vacant s-orbital and π-electrons of the adsorbent and the electron density of the d-orbital of the cation is back donated to the antibonding π-orbitals of the adsorbent. [28-29]The bond strength between sorbent and sorbate depends on:

1) Vacancy in the outer shell s-orbital of the cation located on the surface of the adsorbent.

2) The amount of π-electrons in the target adsorbate molecule and the ease with which these π-electrons can be donated to the s-orbitals of the cation.

3) The amount of d-orbital electrons of the cation and the ease with which they can be donated to the adsorbate molecule.

1.5.2 Direct sulfur-metal interaction

Besides π-complexation, there is another adsorption mechanism between sulfur and adsorbents. Sanchez-Delgado[30] proposed eight possible coordination configurations of thiophene in organometallic complexes as shown in Figure 1-3.[30]

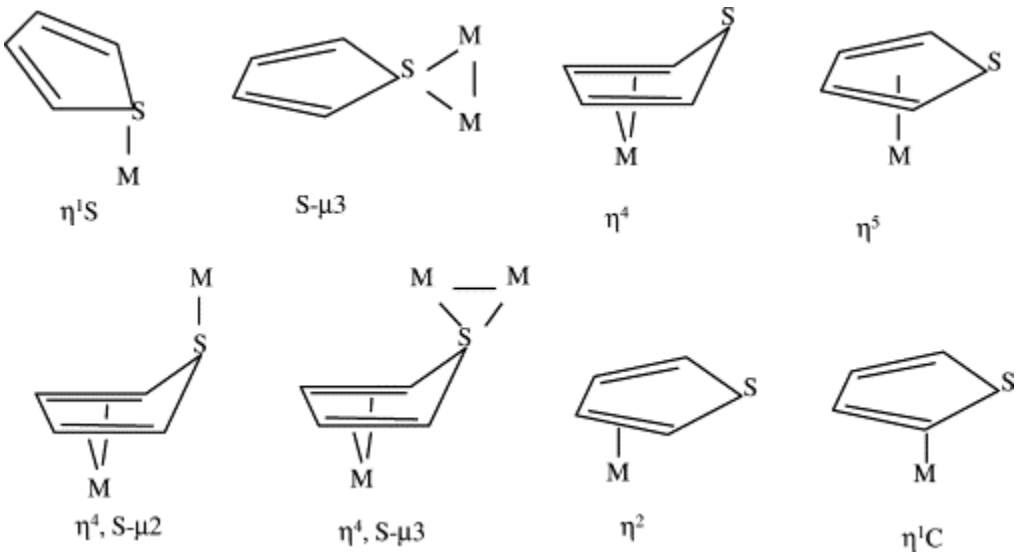

Figure 1-3. Known coordination geometries of thiophene in organometallic complexes, indicating likely configurations of thiophenic compounds on the surface of adsorbents. [30]

1.6 The structure and properties of zeolites

However, only two types of configuration involve the direct sulfur-metal interaction, the η^1S bonding between the sulfur atom and one metal atom, and the S-μ^3-bonding between the sulfur atom and two metal atoms.

Zeolites are microporous aluminosilicates first discovered in 1756 by Swedish mineralogist Cronstedt. Since then, zeolites has been investigated and used as adsorbents because of the molecular sieve property, i.e. the ability to selectively separate molecules form each other based on their size. This is due to a very uniform pore structure of molecular dimensions. According to the International Union of Pure and Applied Chemistry (IUPAC) [31], the pores can be categorized into three classes

based on size: micropores smaller than 2 nm, mesopores between 2 and 50nm and macropores lager than 50nm. The primary building units in zeolites are AlO_4^- and SiO_4 (TO_4 units, T=Al or Si) tetrahedra. They connect with each other by sharing oxygen atoms to form the secondary building units consisting of four, six, or more atoms, as shown in Figure 1-4. [32]

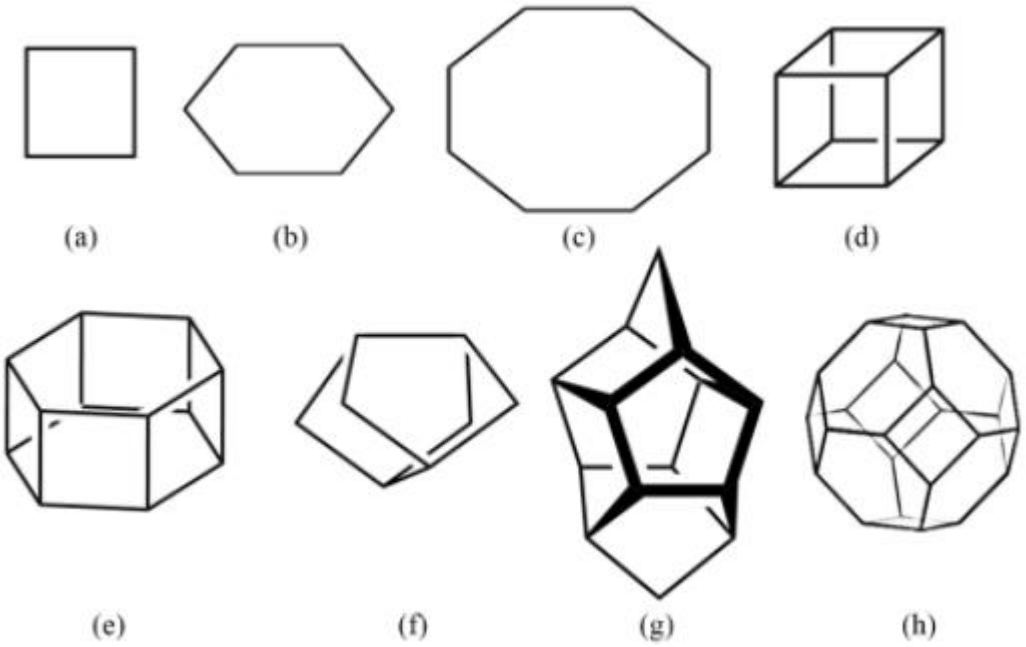

Figure 1-4. The secondary units (SBUs) recognized in zeolite frameworks. (a) Single four rings (S4R), (b) single six rings (S6R), (c) single eight rings (S8R), (d) double four rings (D4R), (e) double six rings (D6R), (f) four five rings, (g) pentasil unit, and (h) sodalite unit, respectively. [32]

The three dimensional structure of zeolites is accomplished by the assembly of the secondary building units. The pore size and shape of zeolites is controlled by the topology of the tetrahedral atoms. Each topology framework has a three letter designation by the International Zeolite Association Commission. [33]

Another important property of zeolites is their ion-exchange ability. The substitution of Si^{4+} by Al^{3+} in the zeolite framework introduces one negative charge

which needs to be balanced by a metal cation or a proton. Theses cations are exchangeable and the adsorptive properties can be tailored by tuning zeolite composition. If the cation is a proton, it acts as Brønsted acid site and the acidity can be modified by tuning Si/Al ratio (SAR). Thus, decreasing SAR in the framework increases the number of acid sites if all the cations were completely occupied by protons. However, the strength of acid sites decreases as the population of acid sites increases due to lower electron density. In addition, it is not appropriate to compare the acidity between zeolites with different topologies based on SAR because the channels, pore dimensions and the accessibility of acid sites are different from each other.

Zeolites with the topologies MWW, FAU and MFI were applied in this work for the sulfur removal from model fuels.

1.7 MWW

1.7.1 3D MWW

In 1990, Rubin er.al [34] first synthesized MCM-22 (Mobil Composition of Matter with sequence number twenty-two) and it was assigned by IZA a three letter code "MWW" (from MCM tWenty tWo). MWW - type layer has a thickness of 2.5nm and composed of two independent pore systems: one is formed by two 12 membered ring (MR) semicups connected at the bottom forming a double 6MR, and the other is 10MR running between the cup, as shown in Figure 1-5.[35]

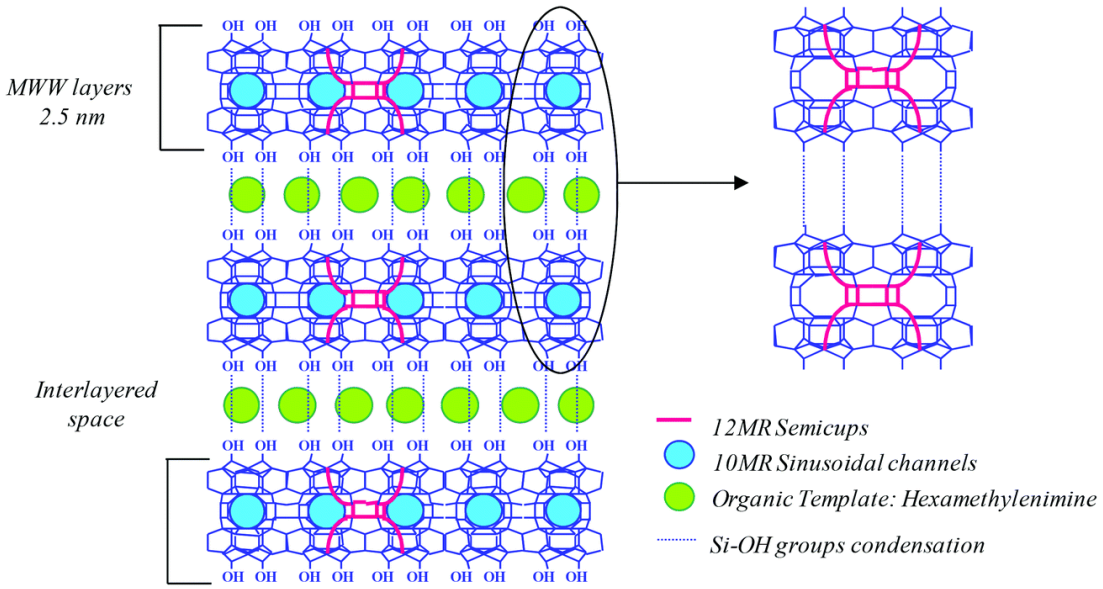

Figure 1-5. Artistic representation of MWW (P) layered precursor.

1.7.2 2D MWW

Generally, the microporous three dimensional structure of zeolites benefits from high selectivity due to the uniform pore size and channels. However, this also impose size constraints on some large reactants or products. MWW type zeolites grows by layer and the reactive silanol groups on each layers can easily condensate after removing organic template by calcination, which results in the low accessibility of active sites. In order to overcome these limitations, many efforts have been directed towards increasing the accessibility to the active sites and decreasing the transportation limitation of bulkier molecules while maintaining some of the characteristic confinement of the microporous zeolites. Conventionally, post-synthetic methods through swelling, intercalation, pillarization, delamination were used to improve the accessibility to the active sites, as shown in Figure 1-6. [36]

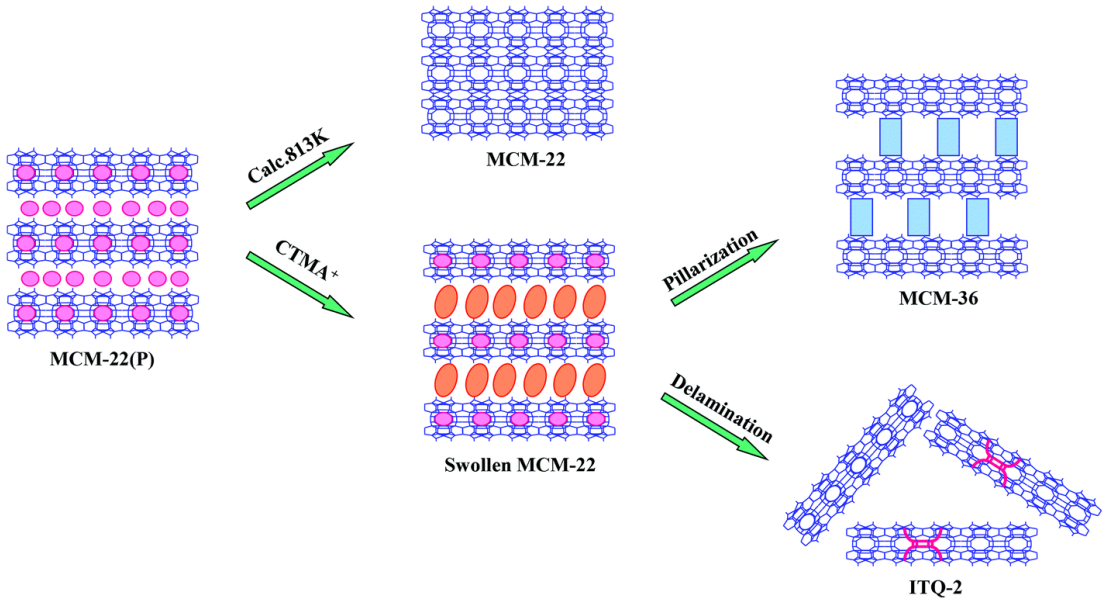

Figure 1-6. Preparation route to obtain delaminated 2D MWW zeolites. [36]

However, these top-down methods involve multiple steps and the strong acidic or basic condition may result in the loss of crystallinity. In a recent research, Corma et al. [37] presented a single-step route for direct synthesis of 2D MWW (DS-ITQ-2) zeolite containing a large portion of MWW monolayers and high preservation of the microporous structure. It has been proven that there is a larger number of external acid sites in 2D MWW zeolite than in 3D MWW. [37]

1.8 FAU

1.8.1 3D FAU

Another most commonly used zeolite in petroleum refinery is zeolite Y. It is a synthetic form of FAU (FAUjasite) type zeolite with silica-to-alumina ratio over 2.5, while in X zeolites it is between 1.5 and 2.5. The stability of the FAU zeolites increases with the SAR of the framework and affected by the type and amount of cations introduced to balance the negative charge.

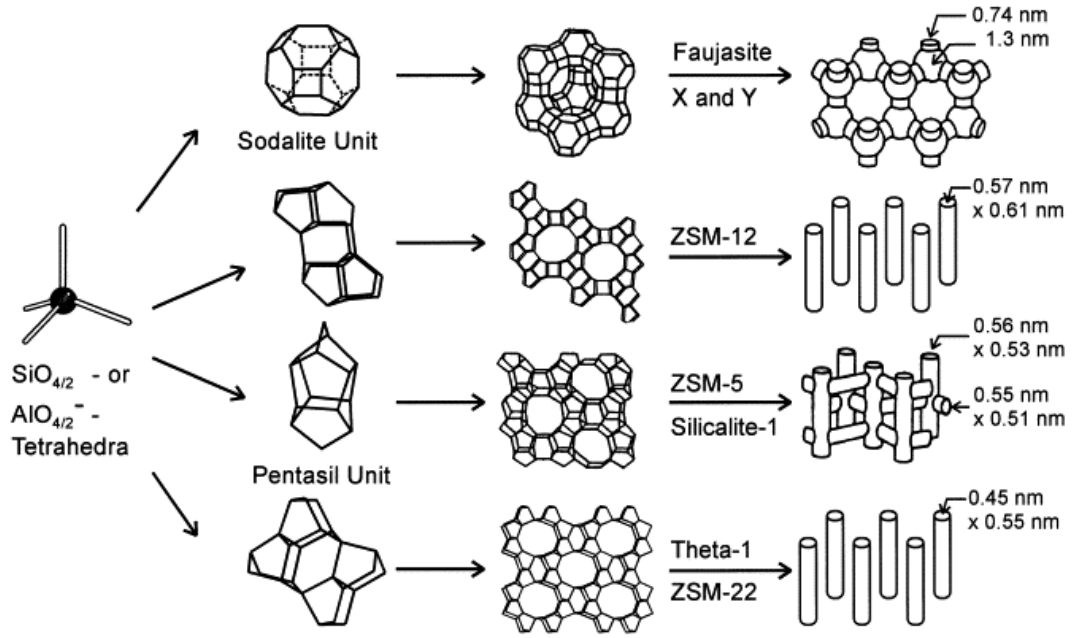

Figure 1-7. Structure of four selected zeolites (from top to bottom: faujasite or zeolite X, Y; zeolite ZSM-12; zeolite ZSM-5 or silicate-1; zeolite Theta-1 or ZSM-22) and their micropore systems and dimensions. [38]

As shown in Figure 1-7 [38], faujasite is formed by the connecting the hexagonal faces of the secondary building unit sodalite, therefore creating a 12 membered-ring called supercage with a diameter of 1.3 nm and a free aperture of 0.74 nm.

Due to the negative charge presented at AlO_4^- units, cations need to be introduced to compensate the negative charge. The locations of these cations are shown in Figure 1-8. [39]

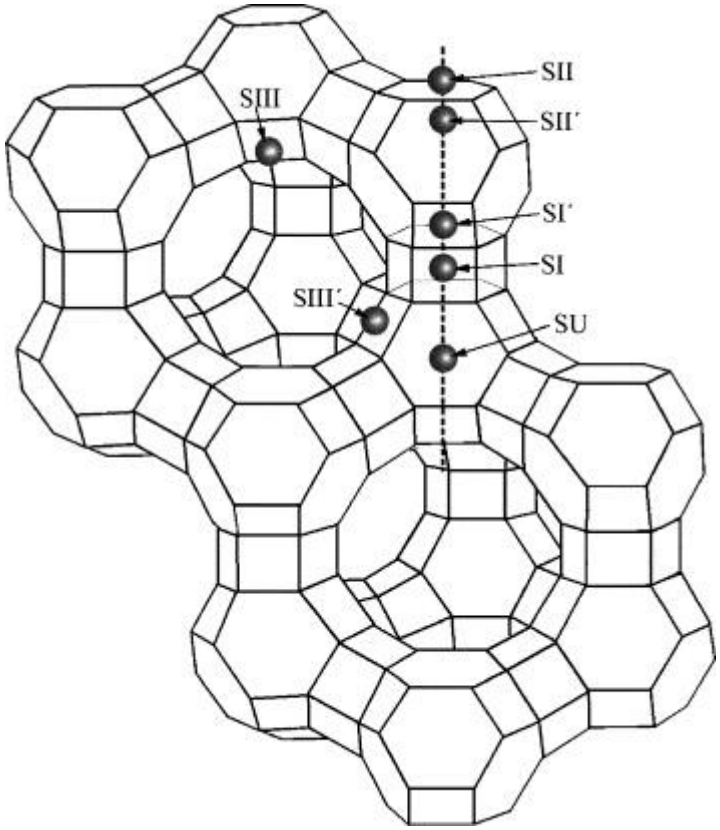

Figure 1-8. Faujasite zeolite framework with cation sites. [39]

Five sites has been found in the work: SI at the center of the double 6-rings, SI' in the sodalite cage, adjacent to a hexagonal ring shared by the sodalite cage and a double 6-ring, SII in the supercage, adjacent to an unshared hexagonal face of a sodalite cage, SII' in the sodalite, adjacent to an unshared hexagonal face, SU near the center of the 12-ring apertures between supercages. These cations are occupied with Na^+ right after synthesis and can be ion-exchange with ammonium nitrate and converted into H form after calcination. For catalytic cracking of crude oil, the cations are usually exchanged with rare earth ions. In this case, the position of cations has an effect on the catalytic performance due to the pore confinement of hexagonal rings for bulkier molecules and therefore reduce the active accessibility.

1.8.2 2D FAU

For microporous low-silica zeolites X, desilication by base is not an appropriate method for introducing mesopores which can reduce diffusion limitation. Therefore, it is very challenging to introduce mesopores into low-silica zeolites. Until 2012, Schwieger et al. [40] successfully synthesized hierarchical X zeolite with a low Si/Al molar ratio of 1.5. In addition, this hierarchical zeolite involves all three (micro-meso-macro) size levels within one particle. As shown in Figure 1-9 [40], there is macroporous interstices up to 200 nm between nanosheet stacks and within each nanosheet there is intracrystalline mesopores with diameter of 7 nm linking by micropores with pore openings of 0.74 nm. Therefore, the accessibility of micropores and external surface area has been greatly improved by the introduction of mesopores and macropores. The hierarchical structure renders mesoporous X zeolites promising materials for adsorption applications and catalytic process involving larger molecules that have diffusion limitation.

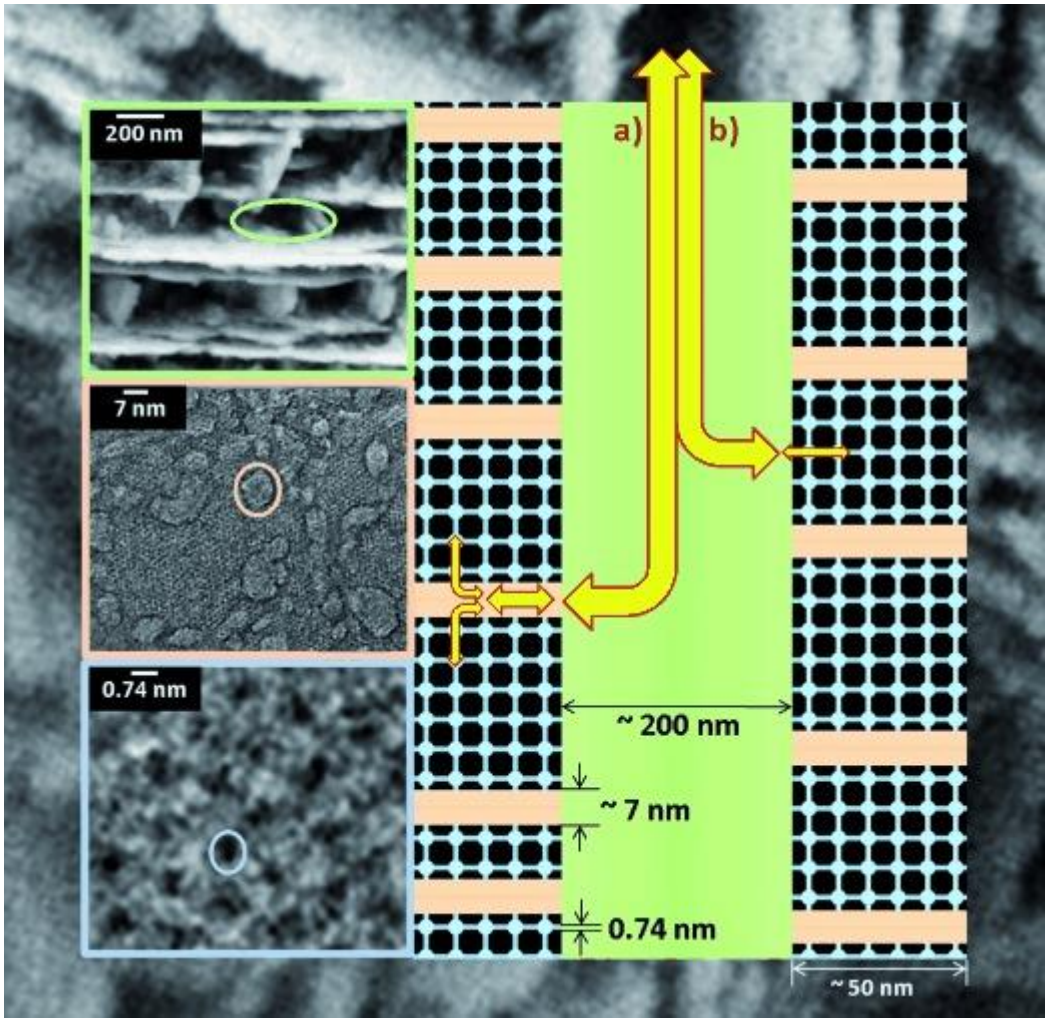

Figure 1-9. Schematic representation of the three different hierarchy levels in the pore structure of the mesoporous zeolite X nanosheet sample, 200 nm= macropores, 7 nm= mesopores, 0.74 nm= micropores; arrows on the right hand side: possible flow paths within the hierarchical pore system: route a) macro-meso-micro, route b) macro-micro. [40]

1.9 MFI

1.9.1 3D MFI

Zeolite ZSM-5 is another widely used zeolite in petroleum refinery as a heterogeneous catalyst for hydrocarbon isomerization reactions. [41] This zeolite was patented by Mobil Oil Corp. in 1975 and was assigned by IZA the code MFI (from Mobil Five). As shown in Figure 1-8, ZSM-5 consists of pentasil units, forming a

structure of straight 10-ring channels with dimensions of 0.56 × 0.53nm and zig-zag channels with dimensions of 0.55 × 0.51nm. The straight channels were linked by the zig-zag channel to form a 3-dimensional 10-membered ring channel system.

1.9.2 2D MFI

Similarly, due to the large amount of micropores, with channel diameters below 1 nm, microporous ZSM-5 zeolites face diffusion limitations which results in low catalytic activity. In order to solve this problem, researchers have been working towards producing ultra-thin zeolites with thickness below 5nm. In 2009, Ryong et al. [42] successfully designed MFI nanosheets that are only 2 nm thick by using bifunctional surfactants, as shown in Figure 1-10. [42]

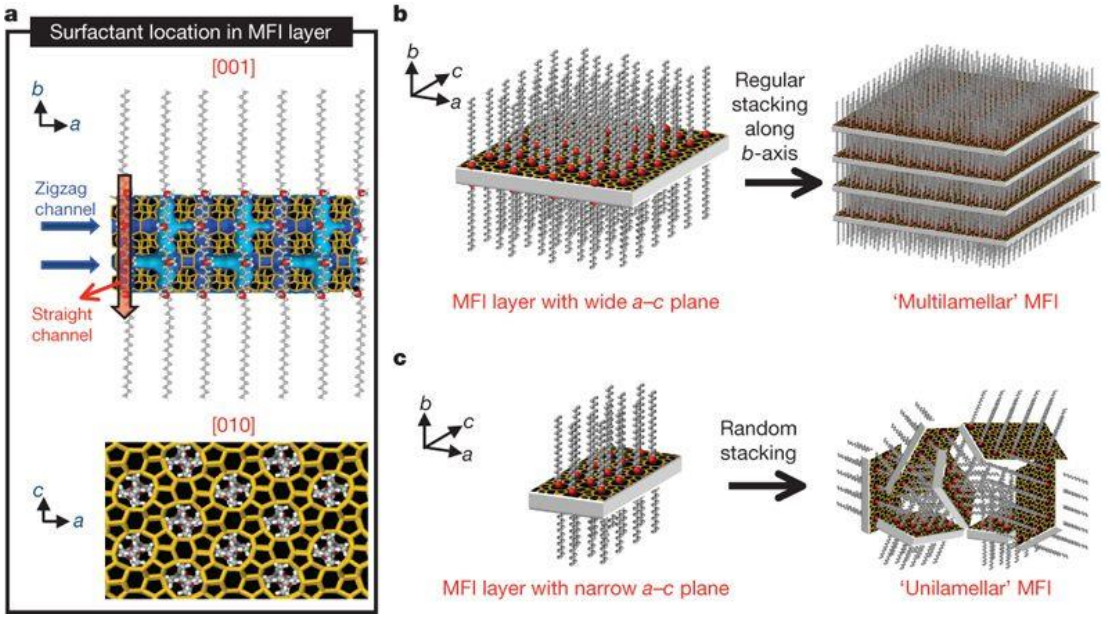

Figure 1-10. (a) Proposed structure model for the single MFI nanosheet. Surfactant molecules are aligned along the straight channel of MFI framework. Two quaternary ammonium groups (indicated as a reed sphere) are located at the channel intersections; one is inside the framework, and the other is at the pore mouth of the external surface. Many MFI nanosheets form either multilamellar stacking along the b-axis (b), or a random assembly of unilamellar structure (c). [42]

Compared with conventional ZSM-5, multilamellar MFI zeolites exhibit higher surface area and higher active sits accessibility due to the single layer nanosheets. In addition, the catalytic performance was investigated with lager organic molecules which has diffusion limitation over conventional ZSM-5. As expected, MFI nanosheets exhibit higher catalytic activities due to the higher accessibility to the active sites located at the mesopore surface which is the external surface of the zeolite layer.

1.10 Motivation and Thesis Outlines

Zeolites are traditional crystalline microporous aluminosilicates which may has transportation limitations for bulky organosulfur compounds such as benzothiophene and dibenzothiophene. Most of the literature has been focused on using 3D Y zeolite with supercages while much less is known about the adsorption behavior of desulfurization performance employing 2D zeolite with higher amount of mesopores which can reduce transportation limitations. This thesis work aimed to investigate the desulfurization performance of metal modified 2D zeolites compared with corresponding 3D zeolites.

Chapter 2. Synthesis of zeolites and adsorption experiments

2.1 Materials

DABCO, Acetonitrile, 1-Bromohexadecane, Tetraethylorthosilicate (TEOS, 98%), ethanol, iodomethane, diethylether, HMI, fumed silica, NaOH (98%), $NaAlO_2$, sodium silicate solution, TPOAC, 1-bromodocosane, N,N,N',N'-tetramethyl-1,6-diaminohexane, acetonitrile, toluene, H_2SO_4, $Al_2(SO)_4 \cdot 16H_2O$.

2.2 Synthesis of 2D materials

2.2.1 Synthesis of 2D MWW

Zeolite 2D MWW was synthesized using a dual organic structure directing agents (OSDA) method published by Prof. Corma's group.[37] In a typical OSDA synthesis, 0.1 mol of DABCO was dissolved in 250mL of Acetonitrile, followed by adding 0.1 mol of 1-Bromohexadecane and kept under stirring at 70℃ overnight. When the solution was cooled down to room temperature, the product was precipitated, filtered and washed with diethylether. Finally, the solid was dried under vacuum at 50℃and denoted as $C_{16}D$. In the second stage, 0.1 mol of $C_{16}D$ was dissolved in 250mL of ethanol and 0.12mol of iodomethane was added. The mixture was covered with alumina foil and stirred at room temperature overnight. Solid was recovered with a rotavap, filtered and washed with diethylether. And the final product was dried under vacuum and denoted as $C_{16}DC_1$.

2D MWW zeolite was hydrothermally synthesized by using the recipe with a composition of $15Na_2O$: $100SiO_2$: $3.3Al_2O_3$: 150HMI: $15C_{16}DC_1$: $40H_2O$. Typically, 0.936g NaOH and 0.541g $NaAlO_2$ were dissolved in 72.04g distilled water. Then,

8.392g $C_{16}DC_1$ was added to the solution while stirring. After the surfactant was completely dissolved, 14.875g HMI and 6g fumed silica were added to the mixture and stirred vigorously for 1h to obtain a gel. The gel was transferred to a 35mL PTFE-lined stainless steel autoclave and rotated at 60rpm and heated at 423K for 7 days. The final product was filtered, washed with distilled water until pH<9. Afterwards, the sample was dried at 373K and calcined at 813K under flowing air for 12h.

2.2.2 Synthesis of 2D FAU

2D FAU was synthesized by using the recipe with a molar composition of $1Al_2O_3$: $3.5Na_2O$: $3SiO_2$: $180H_2O$: 0.06TPOAC reported by Tsapatsis et al.[43] In a typical synthesis, 2g NaOH and 3g $NaAlO_2$ were dissolved in 51.1g deionized water. The sodium aluminate solution was added to 12g sodium silicate solution drop by drop and the mixture were blended for 1h at room temperature. Afterwards, 1.29g TPOAC was added into the mixture and stirred for another 1h. After aging the product statically for 1 day at room temperature, it was crystallized in PTFE bottles at 75 ℃ for 4 days in a convection oven. The solid was collected by centrifugation and washed with DI water until pH<9. The final product was dried at 75℃ overnight and calcined in flowing air by increasing temperature from ambient to 550℃ at 2℃/min and holding for 12h to remove the organic template.

2.2.3 Synthesis of 2D MFI

2D MFI zeolite was hydrothermally synthesized with bifunctional surfactants. [42] The surfactant $C_{22\text{-}6\text{-}6}Br_2$ was synthesized as follows: 15.6g 1-bromodocosane and 68.8g N,N,N',N'-tetramethyl-1,6-diaminohexane were dissolved in 400 acetonitrile/toluene

mixture (1:1 vol/vol) and heated at 70℃for 10h. The .mixture was cooled down to room temperature and followed by filtering and washing with diethylether and drying in a vacuum oven at 50 ℃. In the second stage, 7.56g of the product and 24.6g 1-bromohexane were dissolved in 40.8ml acetonitrile and refluxed for 10h. The mixture was cooled down to room temperature followed by filtering, washing with diethylether and dried in a vacuum oven at 50℃.

2D MFI zeolite was hydrothermally synthesized by using the recipe with a composition of $30Na_2O$: $1.25Al_2O_3$: $100SiO_2$: $10C_{22\text{-}6\text{-}6}Br_2$: $18H_2SO_4$: $4000H_2O$. In a typical synthesis, 1.74g NaOH and 1.26g H_2SO_4 was dissolved in 7.62g and 12.34g DI water respectively. Afterwards, the base was slowly added into the acid solution and the mixture was denoted as solution A. Then 0.5625g $Al_2(SO)_4 \cdot 16H_2O$ was dissolved in solution A followed by adding 15.18g TEOS, and the mixture was stirred at 1000rpm at room temperature overnight. 5.18g $C_{22\text{-}6\text{-}6}Br_2$ was dissolved in 31.26g DI water at 60 ℃ and the solution was added into the mixture prepared in last step and stirred at 1000rpm at room temperature for 2h. Finally, the mixture was transferred into a 35mL PTFE-lined stainless steel autoclave and rotated at 60rpm and heated at 423K for 5 days. The zeolite was collected by centrifugation and washed with DI water until pH<9 and dried at 75℃. The product was calcined at 550℃ for 12h under flowing air to remove organic template.

2.3 synthesis of 3D materials

2.3.1 Synthesis of 3D MWW

3D MWW zeolite was hydrothermally synthesized with a molar composition of 2.7 Na_2O: Al_2O_3: 30SiO_2: 1347H_2O: 15HMI. In a typical synthesis, 1.38g $NaAlO_2$ and 0.9g NaOH were dissolved in 186.3g H_2O. After adding 11.41g HMI and 13.84g fumed silica, the mixture was stir at room temperature for 1h. The gel was transfer to a 35mL PTFE-lined stainless steel autoclave and heated at 423K for 7 days with the autoclave set to tumbling at 60 rpm. The zeolite was recovered by filtration and washed with DI water and dried at 323K. The product was calcined at 823K for 12h under flowing air to remove organic template.

2.3.2 Synthesis of 3D FAU

3D FAU was obtained in the absence of the surfactant with a molar composition of 1Al_2O_3: 3.5Na_2O: 3SiO_2: 180H_2O. Reaction conditions are the same as that of 2D FAU but without adding TPOAC.

2.3.3 Preparation of 3D MFI

Commercial ZSM-5 in ammonium form with a Si/Al ratio 40 was used as 3D MFI zeolites.

2.4 Preparation of H^+ form zeolites

The as-synthesized zeolites were ion-exchanged twice with 1 mol/L aqueous NH_4NO_3 solution at 353K for 3h. After recovering the solid by centrifugation and washing with DI water, the samples were dried at 343K overnight. Finally the zeolite sample in its NH_4^+ form was calcined at 823 K for 12h to decompose NH_3 to H^+.

2.5 Preparation of Ag^+ form zeolites

The silver loaded zeolites were ion-exchanged with 0.1 mol/L aqueous $AgNO_3$ solution at room temperature without exposure of light for 48h. After recovering the solid with centrifugation and washing with large amount of DI water, the samples were dried at 373K overnight in the absence of light. Water and excess amount of $AgNO_3$ were removed by calcination at 723k for 4h.

2.6 Preparation of model fuel

Model fuels containing thiophene and benzothiophene were prepared by dissolving the respective aromatic sulfur compounds in n-octane at different initial concentrations ranging from 200 ppmw to 3500 ppmw. The sulfur compounds were chosen to investigate the pore size effect over sulfur adsorptions performance and n-octane was chosen due to the similarity to the aliphatic hydrocarbons found in diesel fuel.

2.6.1 Thiophene (TP)

Thiophene is a heterocyclic compound consisting of a planar five - membered ring with the formula C_4H_4S. [44-46] It is a colorless liquid with a benzene-like odor at room temperature. Thiophene resembles benzene in most reactions due to the π-electron cloud on the ring and easily undergoes electrophilic reactions in acid medium. In addition, it is a useful monomer for the production of polythiophene. [47]

2.6.2 Benzothiophene (BT)

Benzothiophene is a colorless crystal with an odor similar to naphthalene. It has a larger molecule size compared with thiophene which is only 4.6 Å. The electrophilic

reactions predominately occurs at the 3-position. [47] Table 2-2 listed some physical properties of thiophene and benzothiophene.

Table 2-1. Some physical properties of thiophene and benzothiophene. [47]

Properties	Thiophene	Benzothiophene
Chemical formula	C4H4S	C8H6S
Molar mass (g/mol)	84.14	134.2
Appearance	colorless liquid	colorless crystal
Boiling point (℃)	84.16	221

2.7 Batch adsorption experiments

Acid zeolite H-2D MWW, H-3D MWW, H-2D FAU, H-3D FAU, H-2D MFI, H-3D MFI and corresponding silver ion-exchanged zeolites were screened to adsorb thiophene and benzothiophene in batch experiments at different temperatures and initial concentrations. Prior to desulfurization test, the adsorbents were calcined at 823 K for 12h in order to remove physically adsorbed water. The dried adsorbents (0.015g) were mixed with 0.5g of model fuel in 2 ml vial and stirred at desired temperature for 12h. For silver ion-exchanged adsorbents, the glass vial was covered with Al foil to avoid light. The desulfurized model fuel was separated by filtration and the sulfur concentration of model fuel before and after adsorption were analyzed by gas chromatography using flame ionization detector (FID).

The adsorption capacity (mg of sulfur adsorbed over per gram of zeolite) after reaching equilibrium is calculated as: $q_e = \frac{(C_e - C_0) \times m_{solution} \times 1000}{m_{zeolites}}$

Where, C_0 is the initial concentration of the sulfur compounds in the solution in ppmw, C_e is the concentration of the sulfur compounds in the solution after reaching equilibrium in ppmw, $m_{solution}$ is the amount of model fuel in gram, $m_{adsorbent}$ is the mass of adsorbent in gram. Therefore, the sulfur capacity is valued by the quantity of sulfur compounds adsorbed in gram over per gram of adsorbents. Table 2-2 and 2-3 describe the conditions of gas chromatography analysis applied for the samples.

Table 2-2. Conditions used for separating thiophene from n-octane.

Inlet type	Split inlet
Temperature	180℃
Amount injected	1μl
Split	5:1
Oven temperature	200℃, 5min

Table 2-3. Conditions used for separating benzothiophene from n-octane.

Inlet type	Split inlet
Temperature	280℃
Amount injected	1μl
Split	5:1
Oven temperature	200℃, 10min

The GC calibration curves of all the sulfur compounds were shown as below. The maximum concentration of thiophene and benzothiophene were 7500 ppmw and 5000ppmw, respectively. The standard samples were prepared with concentrations of 600 ppmw, 1250 ppmw, 2000 ppmw, 2500 ppmw, 5000 ppmw and 7500 ppmw. The calibration curves are shown in Figure 2.1. All curves shows a linear response of peak area vs. concentration with R^2 larger than 0.9995.

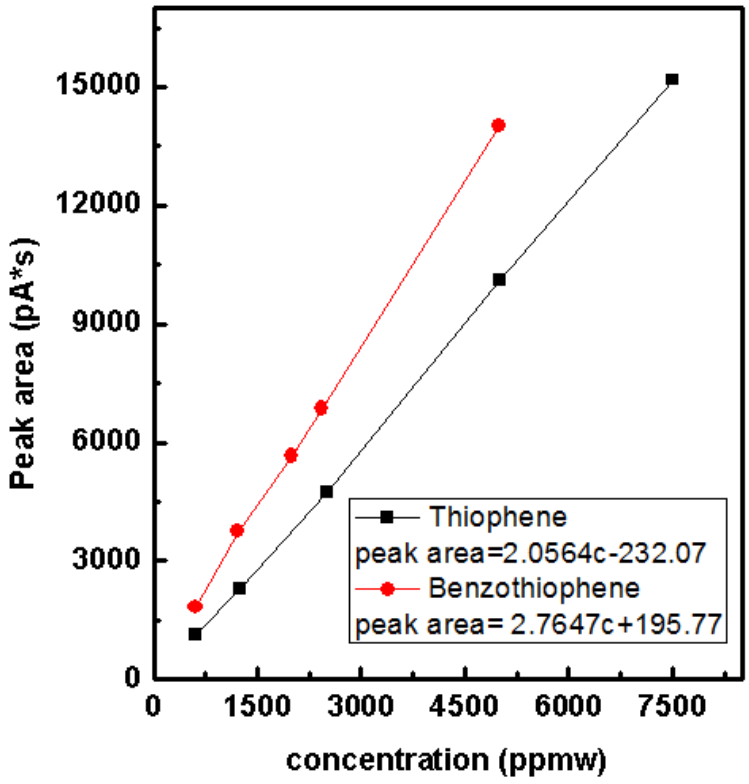

Figure 2-1. Calibration curves of thiophene and benzothiophene.

Chapter 3: Characterizations of zeolites

3.1 Introduction

The morphology of the samples were obtained by scanning electron microscope (SEM). The crystallinity of the samples was determined by X-Ray powder diffraction (XRD). Nitrogen (N_2) adsorption-desorption isotherm was carried out at 87K on an Autosorb-iQ analyzer (Quantachrome Instrument). Prior to the N_2, samples were outgassed at 573K overnight. Evidence of the presence of Ag^+ was obtained from diffuse reflectance ultraviolet-visible spectroscopy (DR-UV-vis). The chemical compositions of Ag+- zeolites were determined by the inductively coupled plasma (ICP) elemental analysis.

3.2 SEM

The morphologies of MWW, FAU and MFI topology zeolites were observed with scanning electron microscope (SEM) and the representative images are shown in Figure 3-1. The MWW-type zeolites (Figure 3.1 (A) & (B)) both have a flake-like morphology in 2D and 3D form, however 2D MWW presents an more open and vertical position of zeolite layers, whereas they are more agglomerated for 3D MWW. The average width of the plate is 0.4 μm.

FAU type zeolites (Figure 3.1 (C) & (D)) consists of octahedral particles with an average size of 5 μm. 3D FAU has a well crystallized smooth surface, whereas 2D FAU present a house-of-cards like nanosheet assemblies. The absence of sponge-like particles indicates the absence of amorphous structure.

MFI type zeolites (Figure 3.1 (E) & (F)) have a plate-like morphology which consists of three dimensionally intergrown nanosheets.

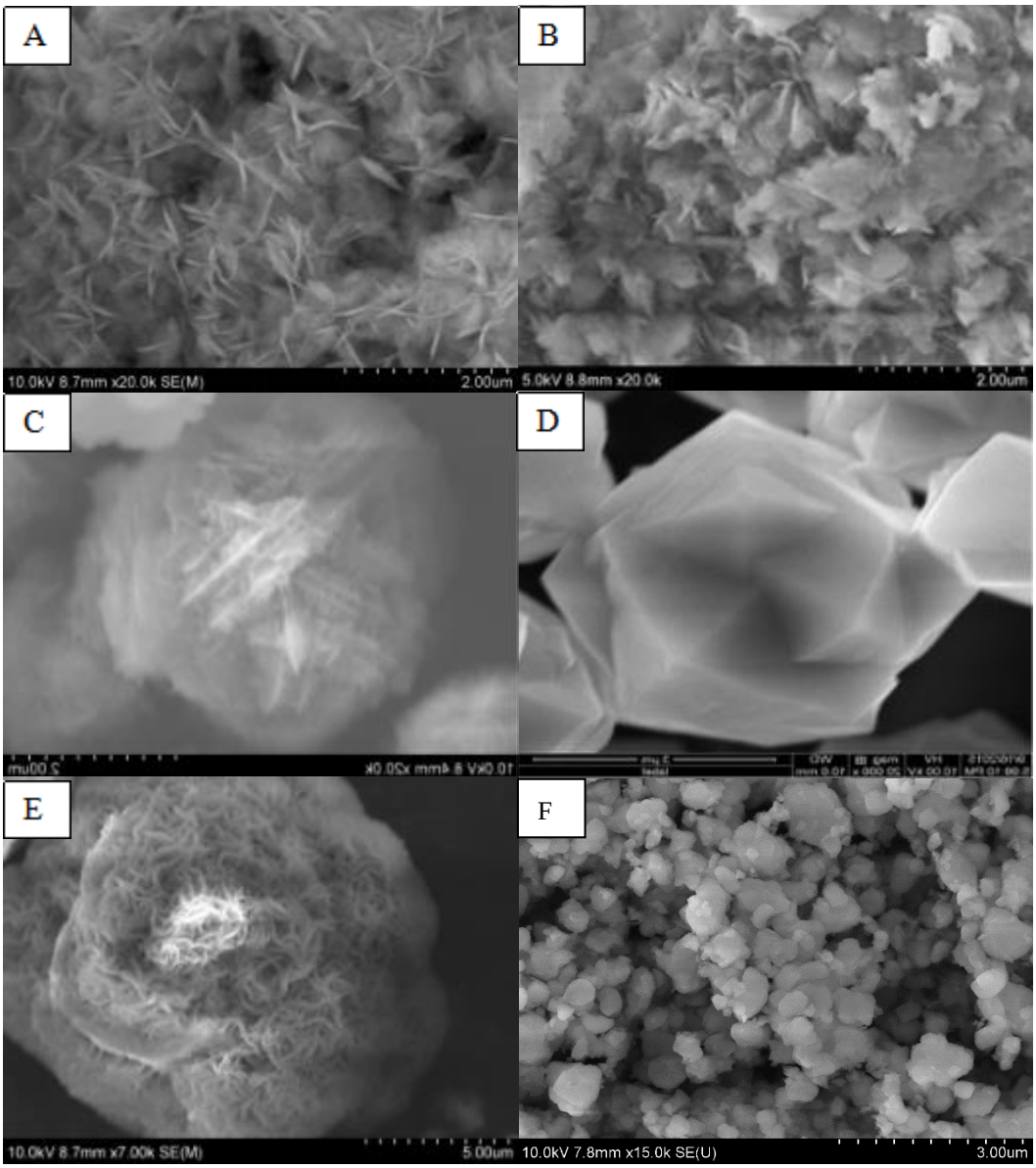

Figure 3-1. SEM images of (A) 2D MWW, (B) 3D MWW, (C) 2D FAU, (D) 3D FAU, (E) 2D MFI and (F) 3D MFI.

3.3 XRD

In order to confirm the crystallinity of the synthesized zeolites, powder X-ray diffraction (XRD) was employed. Figure 3-2 to Figure 3-4 showed the XRD pattern of the synthesized MWW, FAU and MFI zeolites, respectively.

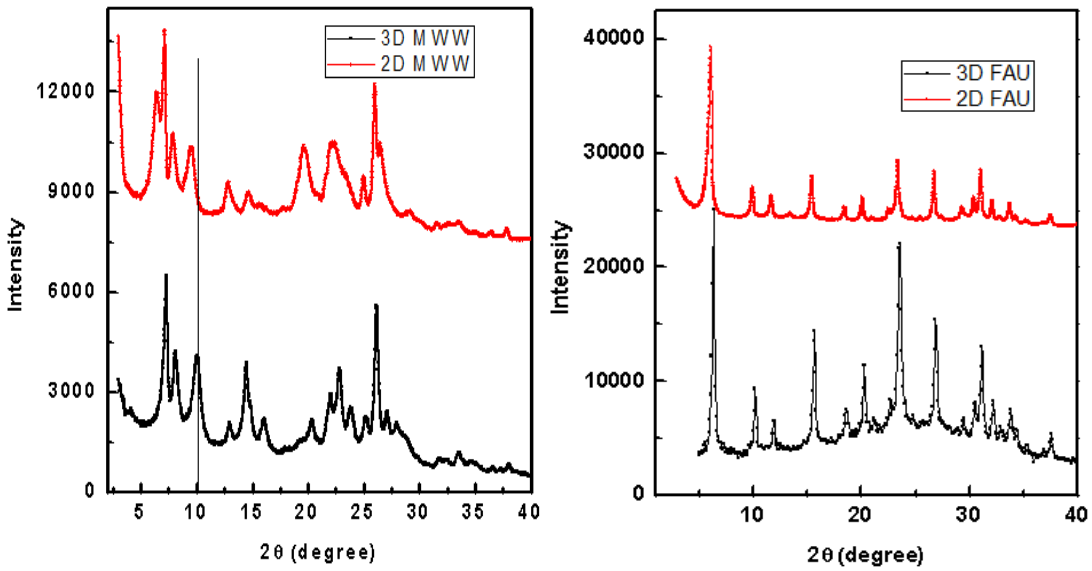

Figure 3-2 & Figure 3-3. XRD pattern for 2D and 3D MWW and FAU zeolites.

3D MWW presents two discrete peaks at 2θ values of 8.1 and 10 °, indicating the interlayer reflections (101) and (102). In the case of 2D MWW, the corresponding peaks shifted to lower 2θ angles due to the higher interlayer spacing based on Bragg's law $n\lambda=2d\sin\theta$. This was caused by the open and vertical structure of MWW layer in 2D MWW.

The XRD pattern for 2D FAU and 3D FAU can be successfully indexed as FAU structure based on the peak position. And the sharp characteristic peaks indicate good crystallinity of synthesized zeolites.

XRD pattern of 2D MFI primarily shows sharp h0l reflections such as 101, 501 and 303. The result indicates that the zeolite has wide a-c planes and extremely small thickness along b-axis.

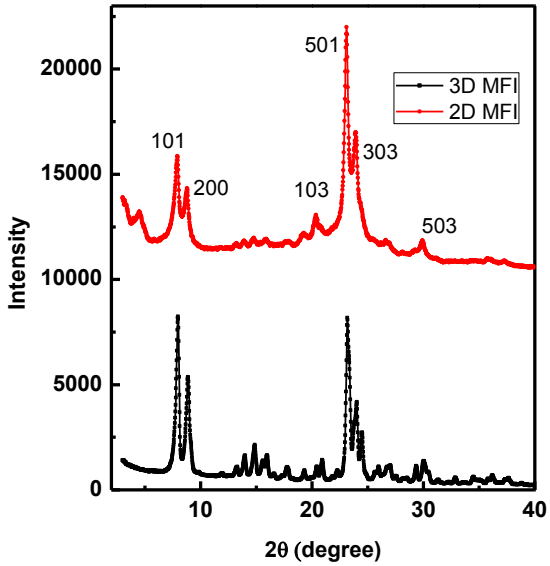

Figure 3-4. XRD pattern for 2D and 3D MFI zeolites

3.4 N_2 adsorption - desorption isotherms

N_2 adsorption - desorption isotherms were carried out to characterize the textural properties of the zeolites, for example, the surface area and porosity. The surface area was calculated based on the multipoint BET method and the micropore volume and total pore volume and pore distribution were calculated using the non-local density functional theory (NLDFT) method on the adsorption branch assuming spherical/cylindrical pore. The textural data and pore distribution of the zeolites were summarized in Table 3-1.

Table 3-1. Textural properties of 2D MWW and 3D MWW zeolites, derived from N_2 isotherms.

Sample	H-3D MWW	H-2D MWW	Ag-3D MWW	Ag-2D MWW
S_{BET} $(m^2/g)^a$	607	659	549	602
S_{ext} $(m^2/g)^b$	194	238	170	199
S_{micro} $(m^2/g)^b$	412	421	379	403
$V_{micro}(cm^3/g)^b$	0.169	0.173	0.155	0.163
V_{total} $(cm^3/g)^c$	0.523	0.545	0.468	0.504
V_{meso} $(cm^3/g)^d$	0.354	0.372	0.313	0.341

[a] Determined from multi-point BET method applied to the N_2 isotherm. [b] Determined from t-plot method applied to the N_2 isotherm. [C] Total pore volume calculated at P/P_0=0.95 applied to the N_2 isotherms. [d] Mesopore volume calculated by mesopore volume = total volume - micropore volume.

The degree of mesoporosity of the 2D MWW in proton form and silver form were confirmed by the shape of N_2 isotherms (see Figure 3-5). 2D MWW has more obvious hysteresis loop formed by the adsorption and desorption curve, indicating higher mesoporosity which can be further proven by the mesopore volume shown in Table 3-1. In addition, 2D MWW has higher external surface area due to the open and vertical structure of MWW layers compared to 3D MWW with agglomerated layers. After ion-exchange with Ag^+, the total pore volume decreased as well as the surface area, which can be attributed to the larger diameter of Ag^+ ions compared to that of H^+. NLDFT pore size analysis in Figure 3-6 shows that MWW zeolites has a broad size distribution ranging from 25 nm to 80 nm.

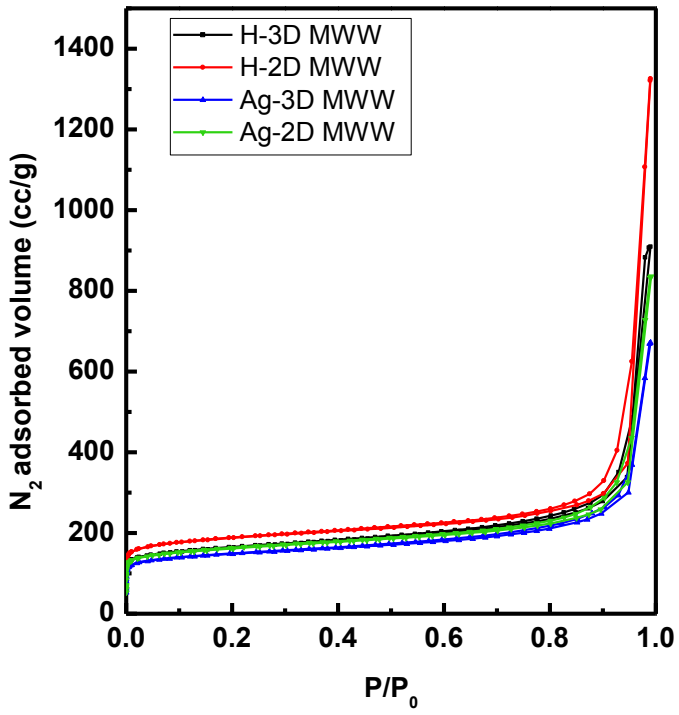

Figure 3-5. N_2 adsorption-desorption isotherms of 2D MWW and 3D MWW

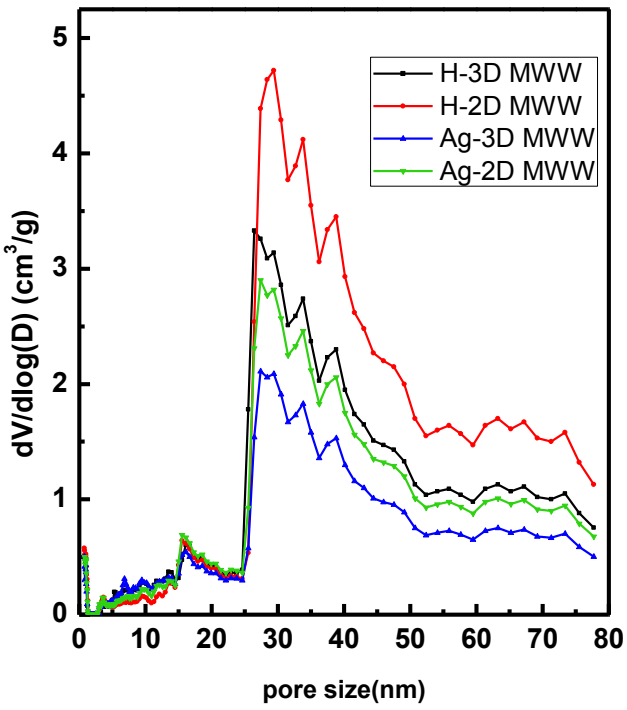

Figure 3-6. Pore distribution curves derived from N_2 sorption (NLDFT on the adsorption branch on the basis of spherical/ cylindrical pore model) of 2D MWW and 3D MWW.

N_2 isotherms and pore size distributions of 2D FAU and 3D FAU were depicted in Figure 3-7 and Figure 3-8. As expected, 3D FAU shows a type I isotherm according to the IUPAC classification, which is typical for microporous materials. In contrast, 2D FAU shows an obvious type IV isotherm which is typical for mesoporous materials. The significant increase of the adsorption branch between 0.4 and 0.95 p/p_0 and the wide hysteresis loop indicate the much higher mesopore volume of 2D FAU that is three times the values determined for 3D FAU, as shown in Table 3-2. The pore size distribution curve of 2D FAU exhibits mesopores with a most frequent pore diameter of around 6 nm, whereas 3D FAU exhibits high microporosity with pore distributed at around 7 Å. The textural properties of FAU samples were listed in Table 3-2. It can be seen that 2D FAU has much higher external surface area and total pore volume than that of 3D FAU, whereas micro surface area is relatively lower due to the sacrifice of micropore during introducing mesopores.

As mentioned before, when a Si^{4+} cation was substituted by a Al^{3+} cation in the zeolite framework, an additional positive charge need to be introduced to keep the charge neutral. The as-synthesized samples were in Na^+ form to compensate the negative charge. The samples can be ion-exchanged by NH_4NO_3 followed by calcination at 550℃ to convert NH_4^+ to H^+. Metal ions like Ag^+ can be introduced by ion-exchange H form zeolites with $AgNO_3$ solution followed by calcination at 450℃ to remove water and impurities.

After ion-exchange with Ag^+, the surface area and pore volume decreased significantly both in 2D FAU and 3D FAU. This may due to the low silica to alumina

ratio of X zeolite (1.5) who contains a large amount of Al. The large amount of Al in the zeolite framework may result in low thermal stability and cause collapse of crystalline structure.

As shown in Table 3-2, the decrease of micropore surface area and the increase of external surface are the evidence of the collapse of micropores and the sacrifice of micropores introduced the disordered mesopores which can be explained by the increasing mesopore volume of Ag-3D FAU. In addition, Ag^+ with larger diameter than that of H^+ can occupy more void space in the cavity and result in the decrease of mesopore volume.

Table 3-2. Textural properties of 2D FAU and 3D FAU zeolites, derived from N_2 isotherms.

Sample	H-3D FAU	H-2D FAU	Ag-3D FAU	Ag-2D FAU
S_{BET} $(m^2/g)^a$	720	673	220	201
S_{ext} $(m^2/g)^b$	71	183	203	136
S_{micro} $(m^2/g)^b$	649	490	17	64
V_{micro} $(cm^3/g)^b$	0.23	0.19	0.007	0.032
V_{total} $(cm^3/g)^c$	0.31	0.46	0.175	0.225
V_{meso} $(cm^3/g)^d$	0.08	0.27	0.182	0.193

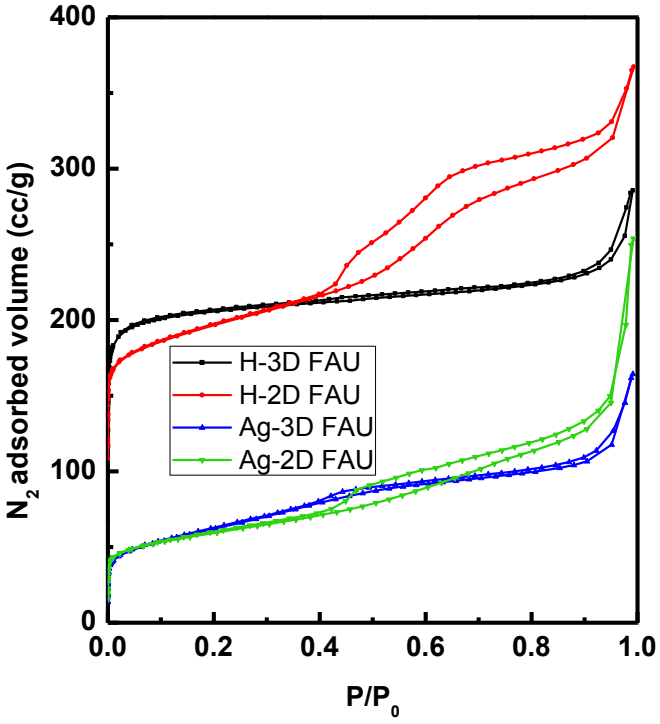

Figure 3-7. N_2 adsorption-desorption isotherms of 2D FAU and 3D FAU.

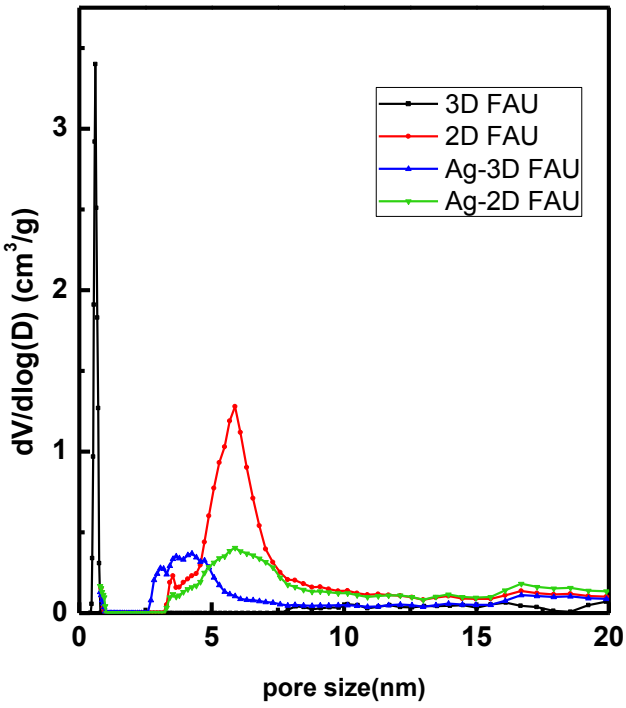

Figure 3-8. Pore distribution curves derived from N_2 sorption (NLDFT on the adsorption branch on the basis of spherical/ cylindrical pore model) of 2D FAU and 3D FAU.

N_2 isotherms and pore size distributions of 2D MFI and 3D MFI were depicted in Figure 3-9 and Figure 3-10. As expected, 2D MFI is highly mesoporous with a pronounced hysteresis loop. The significant increase of the adsorption branch of between 0.4 and 0.95 p/p_0 indicates the much higher mesopore volume of 2D MFI that is around three times the values determined for 3D MFI (see Table 3-3). 3D MFI also shows a narrow hysteresis loop between 0.4 and 0.9 p/p_0. This is because industry usually purposely introduces mesopores to microporous materials to reduce diffusion limitations. The pore size distribution of 2D MFI exhibits mesopores with a most frequent pore diameter of around 6 nm, whereas 3D FAU shows a rather broad pore distribution ranging from 3 nm to 10nm owing to the irregular introduction of mesopores. The textural properties of MFI samples were listed in Table 3-3. It can be seen that 2D MFI has much higher external surface area and total pore volume than that of 3D MFI due to the lamellar structure.

Similarly, the surface area and pore volume slightly decreased after ion-exchange with Ag^+, which can be attributed to the larger diameter of Ag^+.

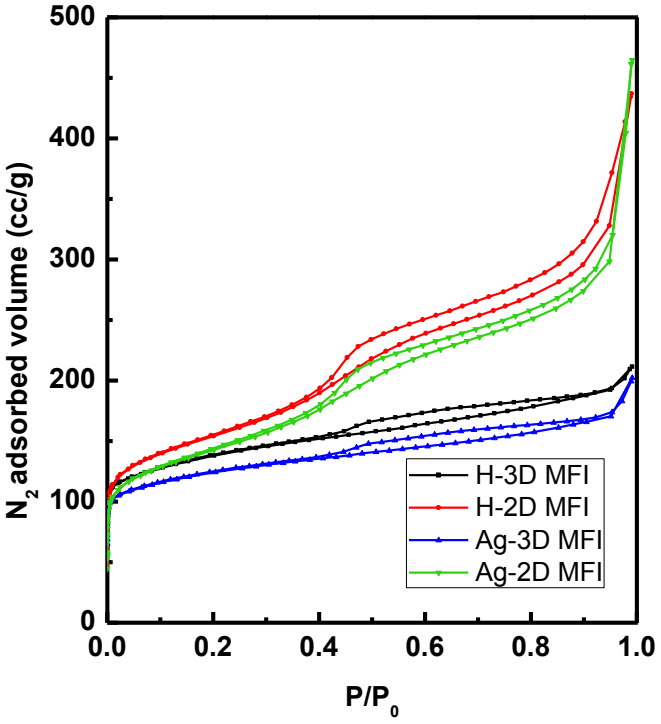

Figure 3-9. N_2 adsorption-desorption isotherms of 2D MFI and 3D MFI.

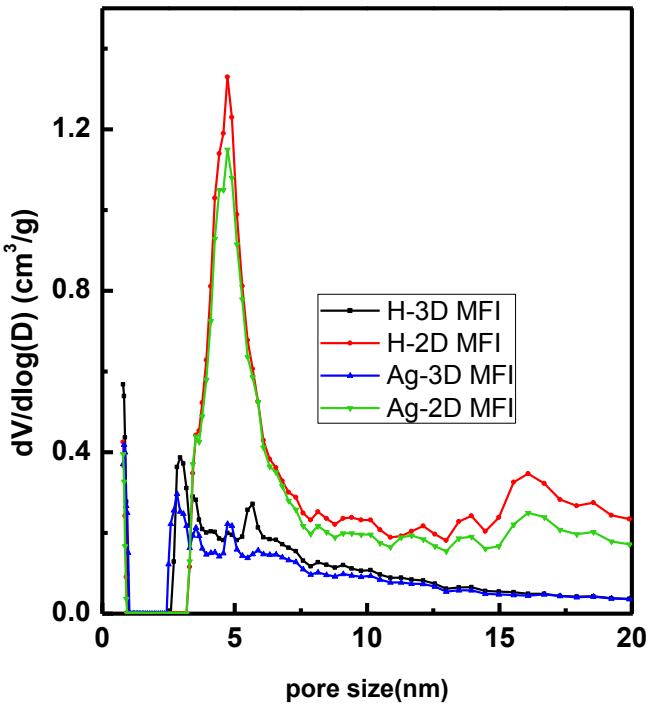

Figure 3-10. Pore distribution curves derived from N_2 sorption (NLDFT on the adsorption branch on the basis of spherical/ cylindrical pore model) of 2D MFI and 3D MFI.

Table 3-3. Textural properties of 2D MFI and 3D MFI zeolites, derived from N_2 isotherms.

Sample	H-3D MFI	H-2D MFI	Ag-3D MFI	Ag-2D MFI
S_{BET} $(m^2/g)^a$	501	552	455	509
S_{ext} $(m^2/g)^b$	171	346	160	337
S_{micro} $(m^2/g)^b$	330	206	295	172
$V_{micro}(cm^3/g)^b$	0.139	0.087	0.121	0.073
V_{total} $(cm^3/g)^c$	0.298	0.507	0.264	0.462
V_{meso} $(cm^3/g)^d$	0.159	0.420	0.143	0.389

3.5 DR UV-Vis

DR UV-vis was carried out to investigate the state of the Ag species. Figure 3-10 to Figure 3-12 showed the UV-Vis diffusive reflectance spectrum of Ag-MWW, Ag-FAU and Ag-MFI and corresponding H^+- zeolites for comparison.

For Ag-MWW, adsorption peaks at 220 and 300 nm were observed. The peak at 220 nm is attributed to the $4d^{10}$ to $4d^9s^1$ transition of highly dispersed Ag^+ ions [48-49], while the lower peak at 300 nm is tentatively assigned to the presence of small $Ag_n^{\sigma+}$ clusters. [50] The adsorption at wavelengths > 390 nm is attributed to metallic silver particles.

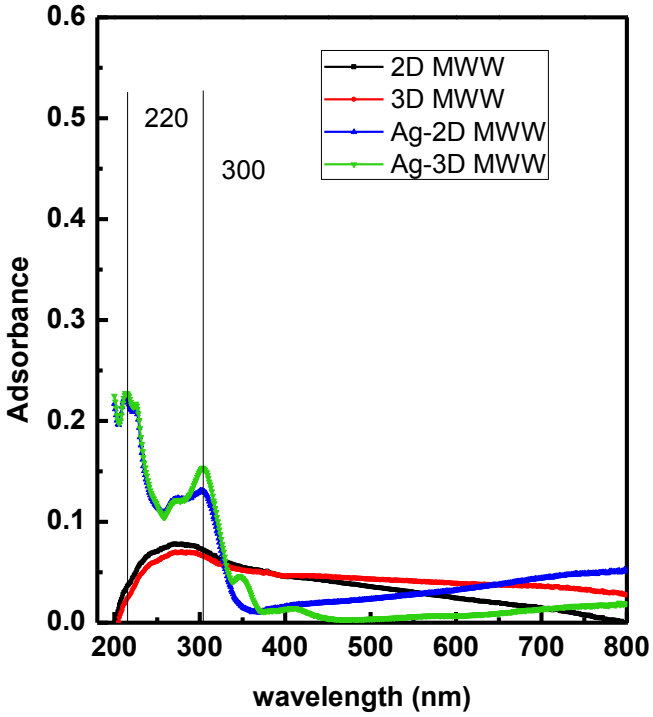

Figure 3-11. UV-Vis diffuse reflectance spectrum of MWW.

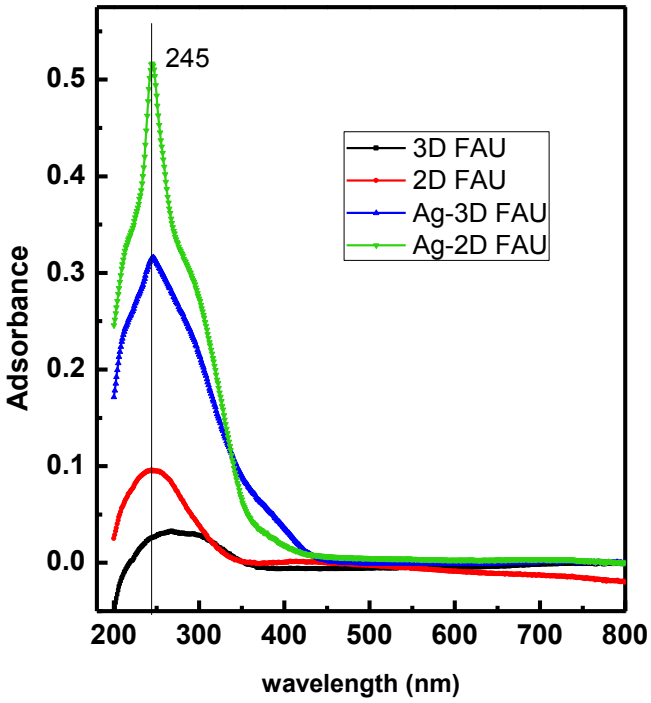

Figure 3-12. UV-Vis diffuse reflectance spectrum of FAU.

The UV-Visible diffuse reflectance spectrum of Ag-FAU shows a high intensity peak at 245 nm. This peak is attributed to Ag^{+} which usually appears between 200 nm and 250 nm. The absence of bands from 400 nm to 800 nm indicates there is negligible amount of Ag_2O. [51]

In the case of Ag-MFI, three adsorption peaks at 214 nm, 227 nm and 255 nm were observed respectively as shown in Figure 3-13. Peaks at 214 nm and 227 nm were attributed to dispersed Ag^{+} while the peak at 255 nm was assigned to small $Ag_n^{\sigma+}$ clusters.

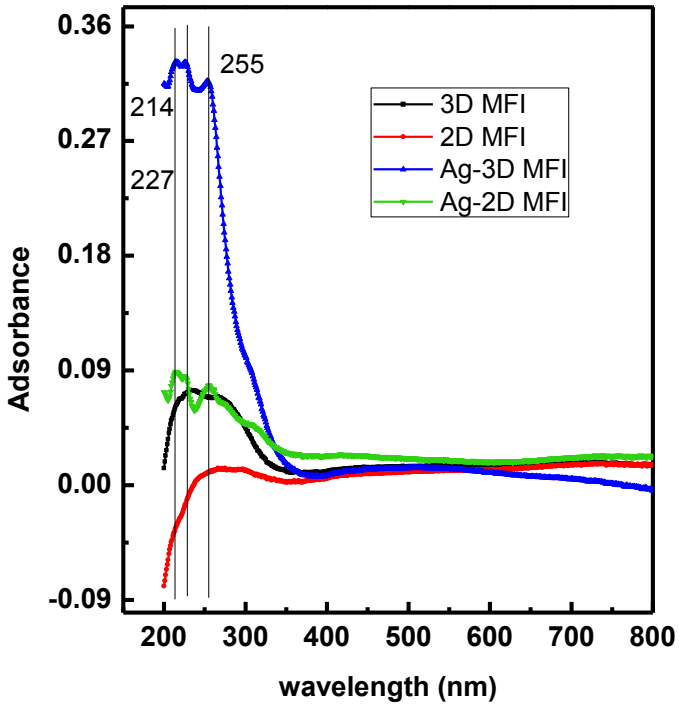

Figure 3-13. UV-Vis diffuse reflectance spectrum of MFI.

3.6 ICP

The chemical compositions of Ag-MWW, Ag-FAU and Ag-MFI were determined by the inductively coupled plasma (ICP) elemental analysis using a high-resolution magnetic sector ICP-MS spectrometer.

Table 3-4. ICP results of Ag-MWW, Ag-FAU and Ag-MFI.

Sample	n(Si)/n(Al)	theoretical n(Si)/n(Al)	Ag mass fraction (wt%)
Ag-2D MWW	20.32	15	0.54
Ag-3D MWW	16.01	15	0.43
Ag-2D FAU	1.54	1.5	0.24
Ag-3D FAU	1.39	1.5	1.61
Ag-2D MFI	47.05	40	0.69
Ag-3D MFI	48.69	40	0.38

As shown in Table 3-4, the experimental SAR values of Ag loaded zeolites are closes to their theoretical values. Theoretically, lower SAR indicates that large amount of Si^{4+} was substituted by Al^{3+} therefore introduced higher amount of negative charges which needs to be balanced by more metal cations. In this case, zeolites with lower SAR are expected to possess higher amount of silver loading. Ag-3D FAU can reach 1.61 wt% of Ag loading while for others, the loading amount is limited within 1 wt%. This may related to the zeolite framework and the procedure applied to introduce Ag.

Chapter 4: Results and discussion

4.1 Introduction

The adsorption of thiophene and benzothiophene, respectively, in n-octane solvent was done using both H^+- and Ag^+-form zeolites in both 2D and 3D structures. Ag^+ was introduced to improve the interaction of Ag^+ and π electrons of double bond in sulfur compounds. 2D zeolites are expected to adsorb more bulky benzothiophene due to the higher accessibility to active sites introduced by mesopores.

4.2 Thiophene adsorption

4.2.1 H^+-zeolites

The H^+- zeolites used throughout this work were prepared by ion-exchange of synthesized zeolites in Na^+ form with NH_4NO_3 followed by calcination except for H-ZSM5 which was directly obtained from commercial NH_4-ZSM-5 by calcination. Thiophene adsorption capability of these zeolites were carried out at room temperature and higher temperature. Batch experiments were performed to investigate adsorption isotherm, adsorption capacity and kinetic of adsorption. The rates of adsorption from model fuel were fairly fast. In all cases 4 h was adequate for reaching equilibrium.

Thiophene is a five-membered ring hetero cycles with aromatic character. It is known to easily undergoes electrophilic attack in acidic solutions, forming stable oligomeric compounds.[52] H^+- zeolites are able to induce protonation of unsaturated species through electrophilic attack of the Brønsted acid sites on the π-system with formation of carbocation monomers and further react with excess monomers to produce oligomer[53-57]. The mechanism of thiophene oligomerization were tentatively shown

in Figure 4-1: a thiophene molecule adsorbed on the Brønsted acid site and formed a protonated monomer $C_4H_5S^+$ which further reacted with excess thiophene to generate positively charged oligomers as shown in Figure 4-1 (b), (b`) and (c). [53]

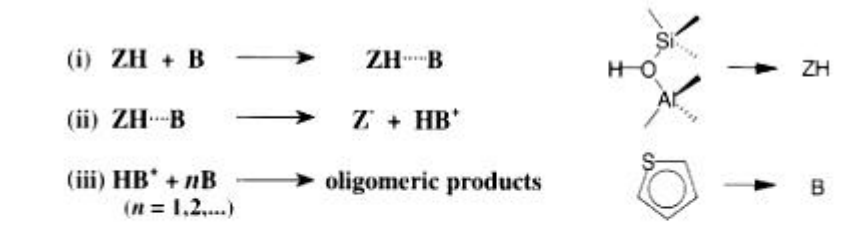

Scheme 2

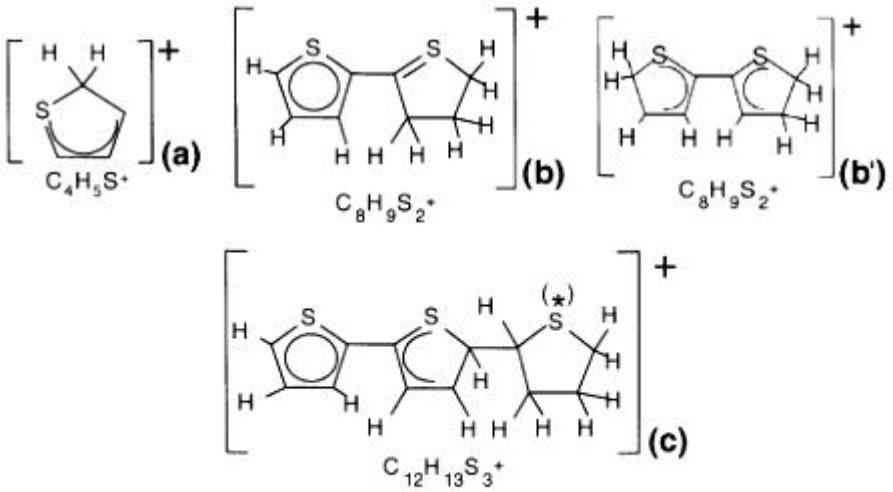

Scheme 3

Figure 4-1. Thiophene oligomer formation over H^+- zeolites. [53]

4.2.2 Thiophene adsorption over H^+- zeolites at room temperature

The adsorption capacity of thiophene from model fuels at 3500 ppmw over H^+-zeolites were shown in Figure 4-2. Based on the theoretical SAR and ICP results of these H^+- zeolites, H-FAU with lowest SAR=1.5 was expected to adsorb higher amount of thiophene, followed by H-MWW (SAR=15) and H-MFI (SAR=40). However, the thiophene adsorption capacity decreases in the order H-MWW > H-MFI > H-FAU, which indicates the intensity of thiophene oligomerization on H^+- zeolites decreases in

the same order. This can be tentatively explained by the effect of acid strength and the structure of the adsorbents. Acid strength of the Si(OH)Al group is affected by the composition of the framework (SiO_2/Al_2O_3 ratio)[58] and zeolite geometry[59]. Among these factor, the zeolite type plays a significant role in affecting acid strength even at a fixed composition of zeolites. It was claimed that the length and angle of Si-O-Al influence Brønsted acid strength and strong acidic zeolites have a range of T-O-T angles (ZSM-5, 137-177 °) than less acidic ones (HY,138-147 °)[60].

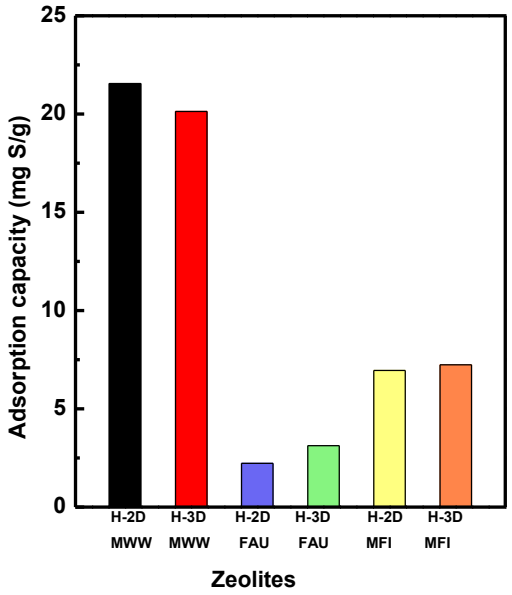

Figure 4-2. Thiophene adsorption capacity over different zeolites at 3500 ppmw.

In Geobaldo's [56] work of propene oligomerization, it was found that the intensity of oligomerization is higher on H-ZSM-5 as compared to mordenite that has a higher proton density. They demonstrated that the rapid blockage of the pore entrance by oligomers prevent further diffusion of monomers to interact with the internal Brønsted acid sites. This assumption may be applicable to our result which H-FAU with highest Al content shows the lowest sulfur adsorption capacity.

Thiophene adsorption capacities of 2D and 3D zeolites with different topologies were shown in Figure 4-2 as well. 3D FAU and 3D MFI exhibit higher adsorption capacity whereas 2D MWW has slightly higher sulfur capacity. This may be caused by the higher micropore volume of corresponding 2D or 3D materials, as shown in Table 3-3. As Naonobu proposed [53], strong acid sites have the trend to be found in relatively small micropores.

The Langmuir isotherm model was applied to experimental equilibrium data for the thiophene adsorption over H^+- zeolites as shown in Figure 4-3. The equation of the Langmuir model is given by the following equation: $\frac{C_e}{q_e} = \frac{1}{K_L q_m} + \frac{C_e}{q_m}$

Where C_e is the concentration at equilibrium (ppmw), q_m is the maximum capacity for adsorbents (mg S/g), q_e is the adsorption capacity for equilibrium concentration (mg S/g) and K_L is the Langmuir adsorption equilibrium constant, representing the affinity between the adsorbent and adsorbate. The values of K_L and q_m are calculated from the intercept and slope of the linear plot of (C_e/q_e) versus C_e.

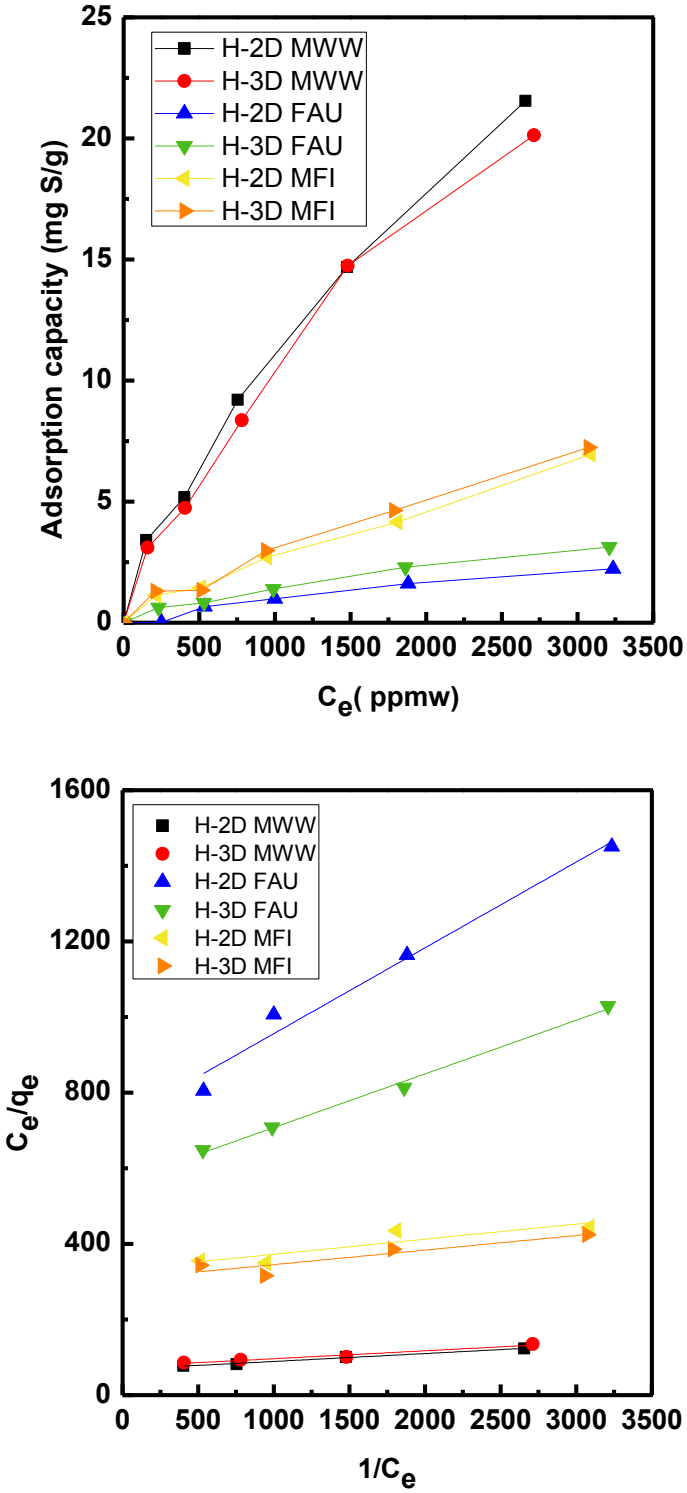

Figure 4-3. Equilibrium adsorption isotherms of thiophene (top) and Langmuir model linear fitting (bottom) over H-2D MWW, H-3D MWW, H-2D FAU, H-3D FAU, H-2D MFI and H-3D MFI materials. (adsorbents mass: 0.015g; model fuel mass, 0.5g; adsorption temperature, 27℃; adsorption time, 12h)

Figure 4-3 (top) shows the relationships of q_e (the adsorptive amount of thiophene per gram of zeolites at equilibrium, mg S/g) against C_e (the concentration at equilibrium (ppmw). As shown in Figure 4-3, initially, q_e increases sharply with an increase of C_e, then increased slightly slowly after 200 ppmw. Eventually, H-FAU almost reached a plateau around 3500 ppmw. However, for H-MWW and H-MFI, they still show a obvious increasing trend around 3500 ppmw. The overall adsorption capacity follows the order H-2D MWW > H-3D MWW > H-3D MFI > H-2D MFI > H-3D FAU > H-2D FAU.

The plot of (C_e/q_e) against C_e shows a good linear relationship, as shown in Figure 4-2 (bottom). K_L and q_m were calculated on the slopes and interceptions of the straight lines and the corresponding regression coefficients are given in Table 4-1.

Table 4-1. Langmuir isotherm parameters for thiophene adsorption over H^+- zeolites at 27℃.

Adsorbents	K_L	q_m	R^2
H-2D MWW	0.000306	47.84	0.9938
H-3D MWW	0.000276	47.84	0.9653
H-2D FAU	0.000221	5.39	0.9784
H-3D FAU	0.000250	7.05	0.9952
H-2D MFI	0.000120	25.00	0.8073
H-3D MFI	0.000125	25.90	0.8347

Table 4-1 shows that H-2D MWW has maximum values of q_m and K_L, while H-2D FAU shows the lowest one, indicating H-2D MWW has a highest capacity for thiophene than the others. In addition, 2D MWW shows higher K_L compared with 3D MWW, indicating higher affinity with thiophene, which can be attributed to the higher amount of micropore volume as explained in previous section. The higher K_L of 3D FAU and 3D MFI are also consistent with the micropore volume of corresponding materials shown in Table 3-1 to 3-3.

4.2.3 Thiophene adsorption over H^+- zeolites at elevated temperature

The sulfur adsorption isotherm was also carried out at 57℃ to investigate the effect of temperature in adsorption process. Figure 4-4 (top) shows the adsorption isotherms over different H^+- zeolites at 57℃.

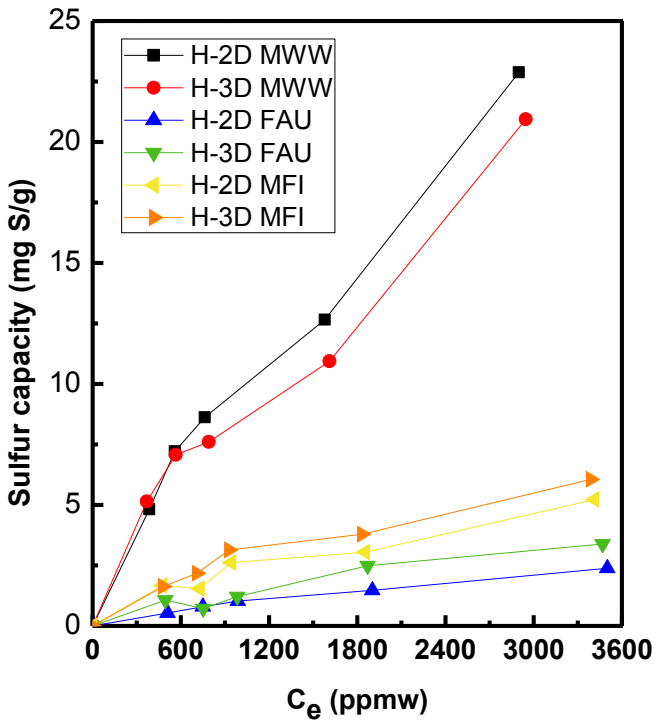

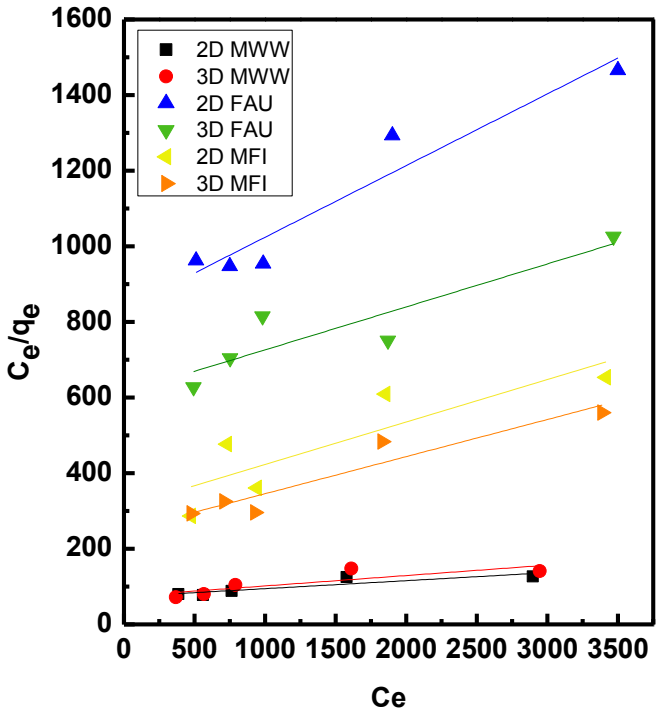

Figure 4-4. Equilibrium adsorption isotherms of thiophene (top) and Langmuir model linear fitting (bottom) over H-2D MWW, H-3D MWW, H-2D FAU, H-3D FAU, H-2D MFI and H-3D MFI materials. (adsorbents mass: 0.015g; model fuel mass, 0.5g; adsorption temperature, 57℃; adsorption time, 12h)

The parameters of Langmuir isotherm at 57 ℃ over H^+- zeolites were listed below.

Table 4-2. Langmuir isotherm parameters for thiophene adsorption over H^+- zeolites at 57℃.

Adsorbents	K_L	q_m	R^2
H-2D MWW	0.000445	47.39	0.8096
H-3D MWW	0.000756	36.36	0.7116
H-2D FAU	0.035910	5.27	0.9260
H-3D FAU	0.012904	8.80	0.8267
H-2D MFI	0.012611	8.90	0.7368
H-3D MFI	0.009643	10.18	0.9089

At elevated temperature, the overall trend remains the same order that H-MWW has highest sulfur capacity followed by MFI and FAU. And these H^+- zeolites did not show obvious increase or decrease in sulfur capacity at higher temperature which means temperature has little effect on adsorption process.

4.2.4 Ag^+- zeolites

Besides H^+- zeolites, Ag^+ was introduced by liquid phase ion-exchange to improve adsorption capacity due to π-complexation. The adsorption of thiophene Ag-MWW, Ag-FAU, Ag-MFI were investigated at 23℃ in a stirred batch system. Figure 4-5 shows the comparison of sulfur capacity over H^+- zeolites and Ag^+- zeolites ones at the same equilibrium concentration.

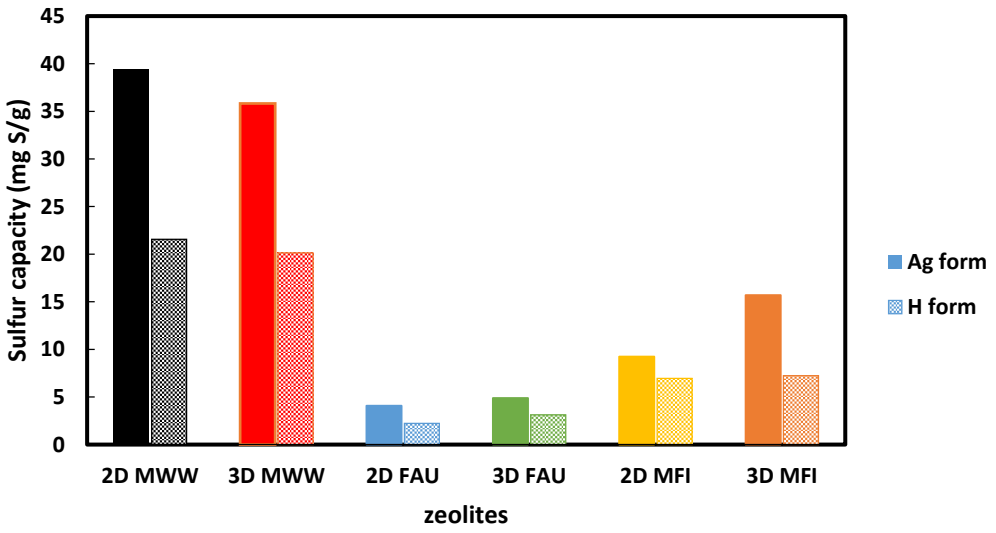

Figure 4-5. Thiophene adsorption capacity of H^+- zeolites and Ag^+-exchanged zeolites at 3500 ppmw.

It is observed that the sulfur capacity increased after loading Ag^+ in all cases. Similarly, the overall trend followed the same order as H^+- zeolites where Ag-2D MWW > Ag-3D MWW > Ag-3D MFI > Ag-2D MFI > Ag-3D FAU > Ag-2D FAU. It is interesting to note that Ag-2D FAU has the highest silver loading amount according

to the ICP data shown in Table 3-4 while it shows the lowest sulfur adsorption capacity. This can be explained by the pore confinement effect of zeolites channels. As shown in introduction, FAU zeolites has a relatively larger pore system consisting of a 0.74×1.2 nm supercage surrounded by 10 sodalites, whereas MWW and MFI have a smaller channel size. The higher sulfur capacity can be attributed to the most comparable pore size of MWW with thiophene molecules size among these three types of zeolites topologies.

In Yongping's[61] work of investigating the pore size dependence of adsorption of thiophene, they found that the maximum adsorption for thiophene can be obtained for average pore size ranging 4.6 to 5Å, suggesting small-pore size zeolites may be suitable for thiophene adsorption. This also can be applied to MWW zeolites.

In addition, for FAU and MFI zeolites, 3D form zeolites performed better than 2D ones, which can be attributed to the higher micropore volume of 2D materials compared with that of 3D materials, as shown in Table 3-1 to 3-3. Since thiophene molecules has small kinetic diameter of 4.6 Å so that it has little diffusion limitation in zeolites pore system. Hence, the micropores of zeolites provides pore confinement and serve as molecular sieves to constrain thiophene molecules in micropores.

Similarly, the Langmuir isotherm model was applied to experimental equilibrium data for the thiophene adsorption over Ag^{+} loaded zeolites as shown in Figure 4-6.

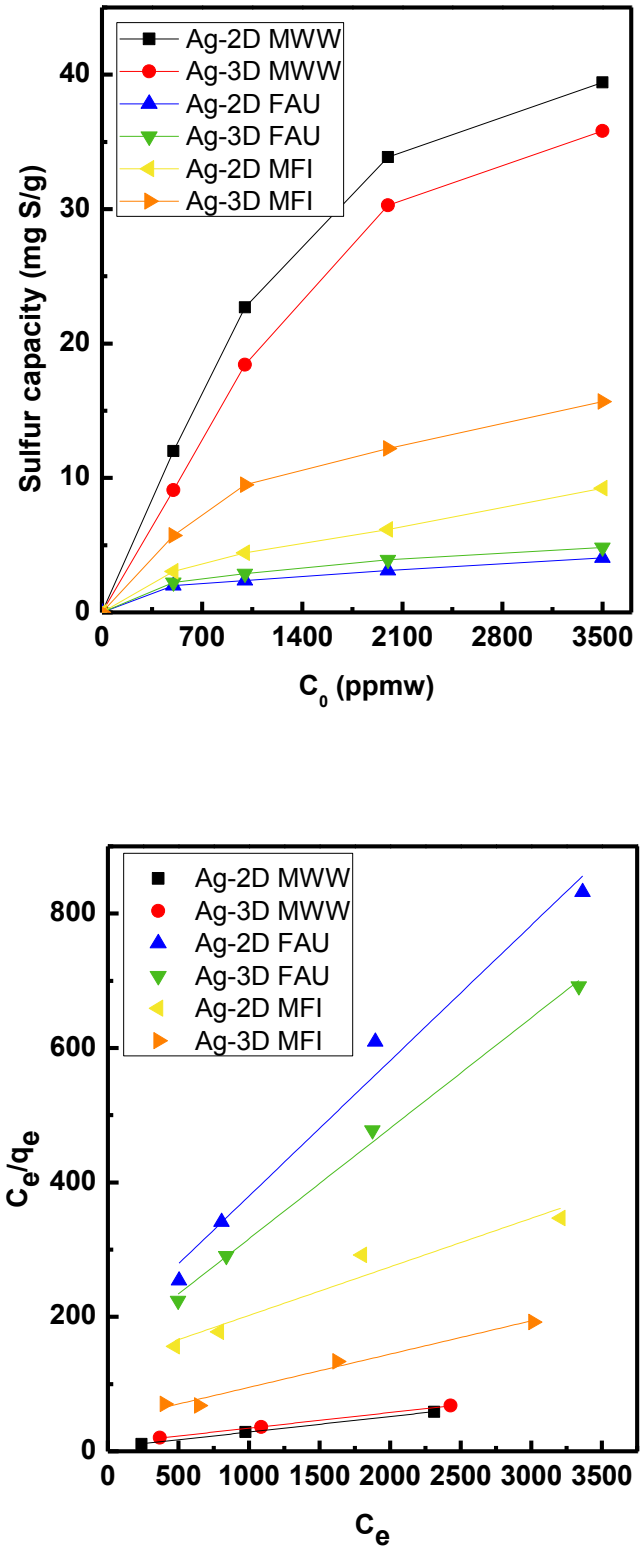

Figure 4-6. Equilibrium adsorption isotherms of thiophene (top) and Langmuir model linear fitting (bottom) over Ag-2D MWW, Ag-3D MWW, Ag-2D FAU, Ag-3D FAU, Ag-2D MFI and Ag-3D MFI materials. (adsorbents mass: 0.015g; model fuel mass, 0.5g; adsorption temperature, 23℃; adsorption time, 12h)

Table 4-3. Langmuir isotherm parameters of thiophene over Ag^+- zeolites at 23℃.

Adsorbents	K_L	q_m	R^2
Ag-2D MWW	0.0231	43.29	0.9993
Ag-3D MWW	0.0233	42.91	0.9997
Ag-2D FAU	0.2014	4.96	0.9824
Ag-3D FAU	0.1644	6.08	0.9964
Ag-2D MFI	0.0722	13.85	0.9444
Ag-3D MFI	0.0495	20.20	0.9834

Table 4-3 shows there is good linearity in Langmuir model fitting. And Ag loaded zeolites shows significantly increased K_L compared with H^+- zeolites, which means there is much higher affinity between adsorbents and thiophene molecules.

Since there is no obvious increase in adsorption capacity over H^+- zeolites at elevated temperature, the adsorption tests over Ag^+ ion exchanged at higher temperature was not further performed.

4.3 Benzothiophene adsorption

Besides small thiophene molecules, sulfur adsorption was also carried out with bulkier organo-sulfur compound like benzothiophene in a batch system. Benzothiophene with a benzene ring may have diffusion limitation over microporous zeolites, hence the pore effect was investigated over 2D and 3D materials.

4.3.1 H^+- zeolites

Similarly, benzothiophene adsorption was first carried out over H^+-zeolites at 23℃. As shown in Figure 4-7, the benzothiophene adsorption capacity followed the order H-2D MWW > H-3D MWW > H-2D MFI > H-2D FAU > H-3D FAU > H-3D MFI. This indicates that MWW zeolites has the most comparable pore size with benzothiophene molecules among these three kinds of zeolites. The higher adsorption capacity of H-2D MFI than H-2D FAU can be attributed to the larger size of benzothiophene which causes diffusion limitation. Compared with H-3D MFI, H-2D MFI possesses higher amount of mesopore which can reduce the diffusion limitation and enable more benzothiophene to adsorb on the active sites. For 3D materials, FAU exhibits higher adsorption capacity than MFI, which can be explained by the higher average pore size of FAU zeolites. Tables 4-4 listed the Langmuir adsorption parameters of benzothiophene, again, H-MCM-22 shows highest maximum capacity of benzothiophene.

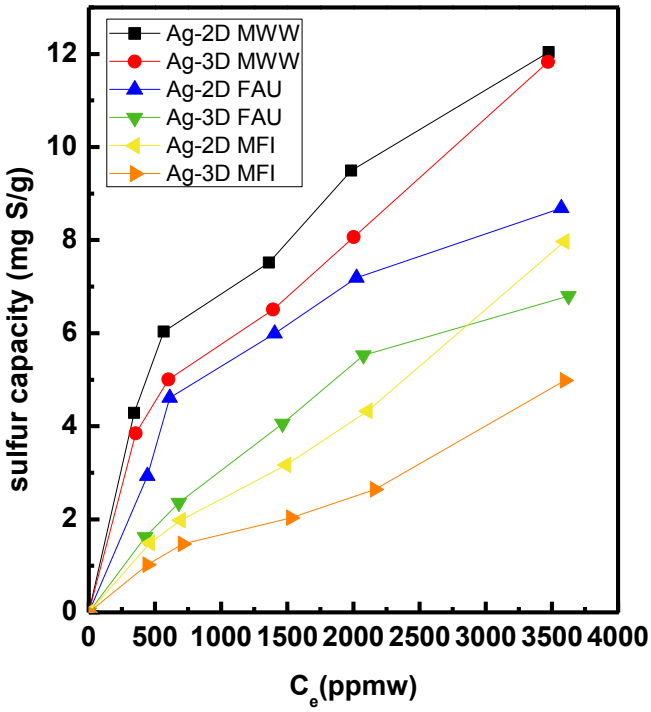

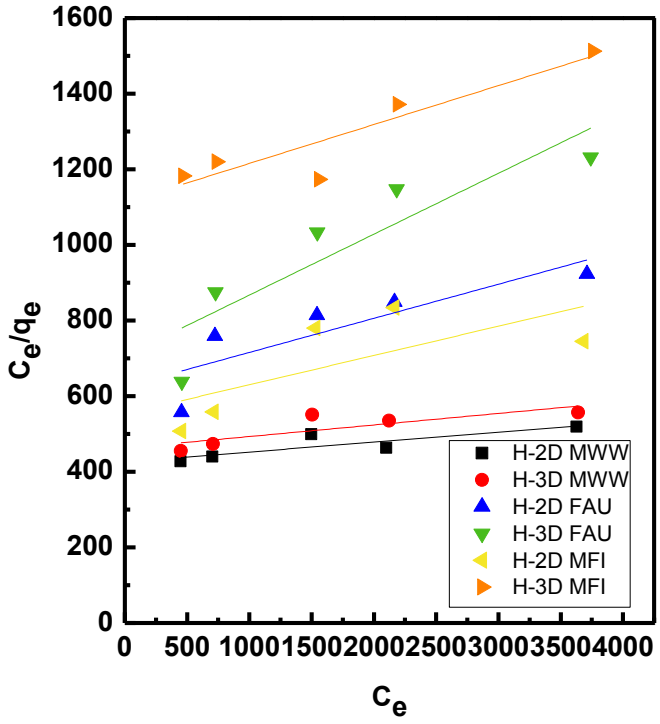

Figure 4-7. Equilibrium adsorption isotherms of benzothiophene (top) and Langmuir model linear fitting (bottom) over H-2D MWW, H-3D MWW, H-2D FAU, H-3D FAU, H-2D MFI and H-3D MFI materials. (adsorbents mass: 0.015g; model fuel mass, 0.5g; adsorption temperature, 23℃; adsorption time, 12h)

Table 4-4. Langmuir isotherm parameters of benzothiophene over H^+- zeolites at 23℃.

Adsorbents	K_L	q_m	R^2
H-2D MWW	0.0000066	36.23	0.9969
H-3D MWW	0.0000065	32.78	0.6959
H-2D FAU	0.0001442	11.08	0.7218
H-3D FAU	0.0002297	6.21	0.8071
H-2D MFI	0.0001400	12.91	0.4867
H-3D MFI	0.0000085	10.44	0.8341

4.3.2 Ag^+ - zeolites

Besides benzothiophene adsorption over H^+- zeolites, the performance tests were also carried out over Ag^+- zeolites which are expected to show higher capacity due to π complexation.

Figure 4-8 shows the benzothiophene adsorption capacity of H^+- zeolites and Ag^+- zeolites. As expected, silver loaded zeolites exhibit better performance and the capacity can be increased up to 70%.

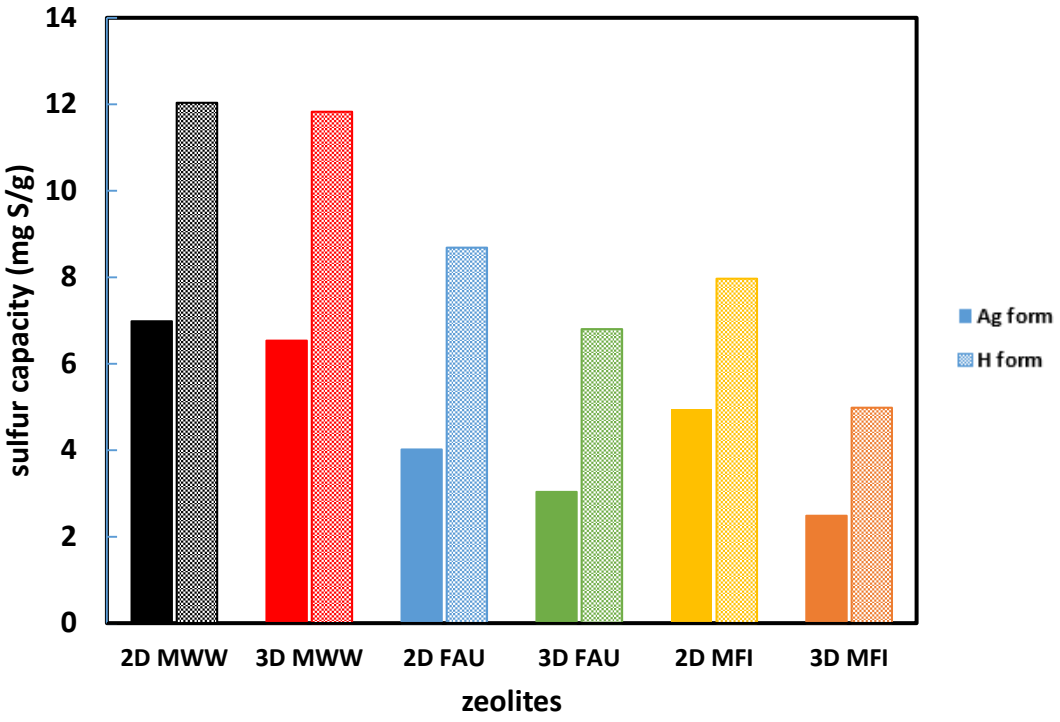

Figure 4-8. Benzothiophene adsorption capacity of H^+- zeolites and Ag^+- zeolites.

The benzothiophene adsorption isotherms and Langmuir isotherm parameters were shown in Figure 4-9 and Table 4-5, respectively.

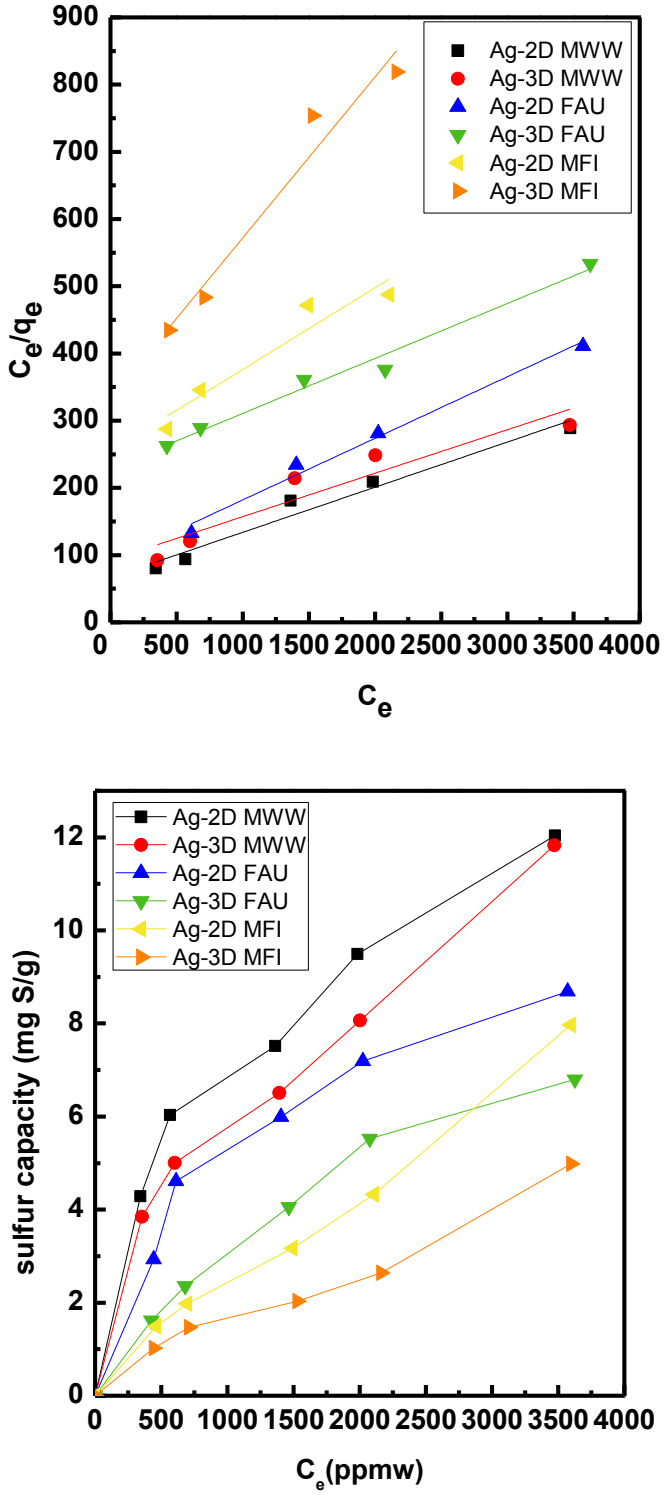

Figure 4-9. Equilibrium adsorption isotherms of benzothiophene (top) and Langmuir model linear fitting (bottom) over Ag-2D MWW, Ag-3D MWW, Ag-2D FAU, Ag-3D FAU, Ag-2D MFI and Ag-3D MFI materials. (adsorbents mass: 0.015g; model fuel mass, 0.5g; adsorption temperature, 23℃; adsorption time, 12h)

Table 4-5. Langmuir isotherm parameters of benzothiophene over Ag^+ - zeolites at 23℃.

Adsorbents	K_L	q_m	R^2
Ag-2D MWW	0.001007	14.88	0.9679
Ag-3D MWW	0.000699	15.45	0.9001
Ag-2D FAU	0.001012	10.91	0.9875
Ag-3D FAU	0.000357	12.22	0.9829
Ag-2D MFI	0.000476	8.23	0.9215
Ag-3D MFI	0.000720	4.17	0.9605

As shown in Figure 4-9, the benzothiophene adsorption capacity follows the order Ag-2D MWW > Ag-3D MWW > Ag-2D FAU > Ag-3D FAU > Ag-2D MFI > Ag-3D MFI. MWW zeolites with the comparable pore size with benzothiophene again shows the highest capacity. However, unlike the H^+- zeolites, Ag-2D FAU exhibits better performance than Ag-2D MFI which can be attributed to the higher amount of silver loading. 2D materials with higher mesopores always show higher capacity due to the reduction of diffusion limitation.

In addition, a comparison was made between thiophene and benzothiophene adsorption over Ag loaded zeolites. As shown in Figure 4-10, Ag loaded MWW and MFI adsorbed much lower amount of benzothiophene compared with that of thiophene, whereas FAU adsorbed more benzothiophene molecules. This can be attributed to the larger pore size of FAU, up to 0.7 ×1.2 nm. In this case, benzothiophene has more

chance to be adsorbed on the active sites, whereas smaller thiophene molecules tends to diffuse through the pores without adsorption.

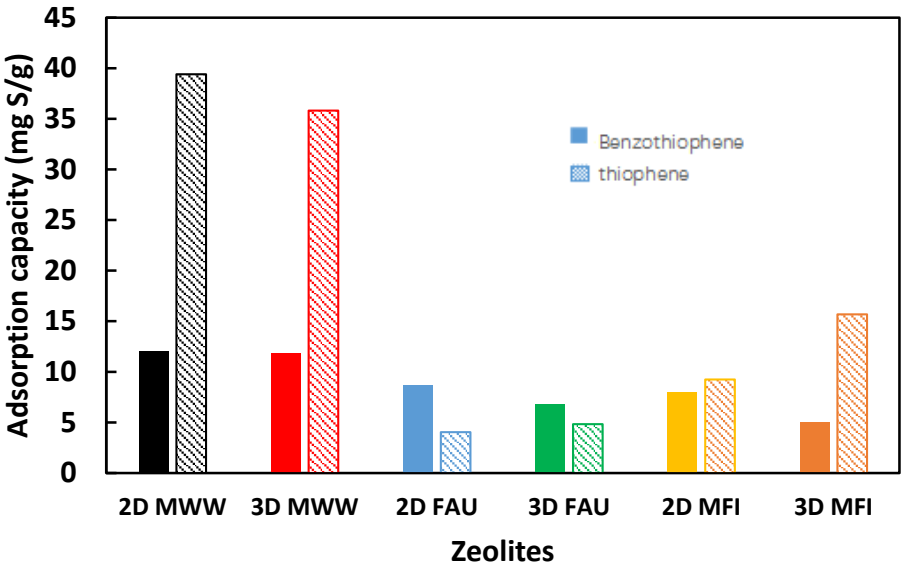

Figure 4-10. Thiophene and benzothiophene adsorption over Ag^{+}-zeolites at same conditions.

Chapter 5: Conclusions and future work

5.1 Conclusion

In this study, we explored the effect of pore size on organo-sulfur removal by using 2-dimensional (2D) and 3D zeolites at room temperature and ambient pressure. Our experimental results, though still preliminary, demonstrated that the pore size of zeolites plays a crucial role in sulfur adsorption.

We firstly synthesized three zeolite frameworks (MFI, MWW and FAU) in both 2-dimensional (2D) and 3D structures. Ion-exchange of proton-form zeolite (H^+-zeolite) was done to introduce silver ions (Ag^+) for the Ag^+-zeolite adsorbent preparation. The physicochemical properties of these adsorbents were characterized. The adsorption of thiophene and benzothiophene, respectively, in n-octane solvent was done using both H^+- and Ag^+-form zeolites in both 2D and 3D structures.

The Ag^+-form zeolites increase the adsorption of thiophene and benzothiophene due to interaction between Ag^+ and π electrons of sulfur compounds, in comparison with that of H^+-form that exclusively due to oligomerization for thiophene adsorption.

The experimental results showed that compared with 3D materials, 2D zeolites with more mesopores adsorbed higher amount of bulkier organo-sulfur compound like benzothiophene. This enhancement is driven by the incorporation of mesopores which provide the access of bulky sulfur compounds to the active sites. For smaller sulfur compound like thiophene, 3D zeolites with higher amount of micropores showed better performance due to the pore confinement effect.

In terms of zeolite framework effects, the thiophene adsorption capacity follows the order of MWW > MFI > FAU for thiophene due to the comparable pore size with thiophene molecules. The benzothiophene adsorption capacity decreases in the order of H-2D MWW > H-MFI > H-FAU for benzothiophene due to the higher mesoporosity of MFI compared with FAU. For Ag^+-zeolites, the benzothiophene adsorption follows the order of Ag-2D MWW > Ag-MFI > Ag-FAU due to the higher amount of Ag^+ loading.

5.2 Future work

5.2.1 Optimization of Ag^+ loading

As shown in the ICP data, the silver loading amount is below 3 wt% which significantly limited the adsorption capacity. An alternative method like wet impregnation of Ag^+ should be explored. In addition, the surface area and pore volume of FAU zeolites were significantly reduced after ion-exchange with $AgNO_3$. The reason behind this reduction should be explored.

5.2.2 Dibenzothiophene adsorption tests

Organo-sulfur compounds like thiophene and benzothiophene adsorption were investigated over 2D and 3D zeolites. However, dibenzothiophene with two benzene rings is the major organic sulfur contaminant in transportation fuels. Hence, the adsorption performance tests need to be carried to further investigate the effect of pore size and contribution of mesopores during adsorption process.

5.2.3 Regeneration tests

Regeneration ability is an important property of adsorbents. In our case, spent zeolites can be regenerate by washing with diethyl ether to remove the adsorbed sulfur compounds. And the stability and reuse-ability should be investigated in the batch system at same conditions.

Reference

1. A. Groysman, Corrosion in Systems for Storage and Transportation of Petroleum Products and Biofuels: Identification, Monitoring and Solutions, Springer Netherlands, 2014.
2. Control of Air Pollution From Motor Vehicles, Tier 3 Motor Vehicle Emission and Fuel Standards. Agency, U. S. E. P., Ed. Federal Register, 2013, vol. 78.
3. de Souza, W. F., Guimarães, I. R., Guerreiro, M. C., & Oliveira, L. C. (2009). Catalytic oxidation of sulfur and nitrogen compounds from diesel fuel. *Applied Catalysis A: General*, *360*(2), 205-209.
4. Eßer, J., Wasserscheid, P., & Jess, A. (2004). Deep desulfurization of oil refinery streams by extraction with ionic liquids. *Green chemistry*, *6*(7), 316-322.
5. McKinley, S. G., & Angelici, R. J. (2003). Deep desulfurization by selective adsorption of dibenzothiophenes on Ag+/SBA-15 and Ag+/SiO 2. *Chemical Communications*, (20), 2620-2621.
6. Li, H., Jiang, X., Zhu, W., Lu, J., Shu, H., & Yan, Y. (2009). Deep oxidative desulfurization of fuel oils catalyzed by decatungstates in the ionic liquid of [Bmim] PF6. *Industrial & Engineering Chemistry Research*, *48*(19), 9034-9039.
7. Zhang, J., Zhu, W., Li, H., Jiang, W., Jiang, Y., Huang, W., & Yan, Y. (2009). Deep oxidative desulfurization of fuels by Fenton-like reagent in ionic liquids. *Green Chemistry*, *11*(11), 1801-1807.
8. Syunyaev, R. Z., Balabin, R. M., Akhatov, I. S., & Safieva, J. O. (2009). Adsorption of petroleum asphaltenes onto reservoir rock sands studied by near-infrared (NIR) spectroscopy. *Energy & Fuels*, *23*(3), 1230-1236.
9. Sarda, K. K., Bhandari, A., Pant, K. K., & Jain, S. (2012). Deep desulfurization of diesel fuel by selective adsorption over Ni/Al2O3 and Ni/ZSM-5 extrudates. *Fuel*, *93*, 86-91.
10. Song, C. (2003). An overview of new approaches to deep desulfurization for ultra-clean gasoline, diesel fuel and jet fuel. *Catalysis today*, *86*(1-4), 211-263.
11. Campos‐Martin, J. M., Capel‐Sanchez, M. D. C., Perez‐Presas, P., & Fierro, J. L. G. (2010). Oxidative processes of desulfurization of liquid fuels. *Journal of Chemical Technology & Biotechnology*, *85*(7), 879-890.
12. Song, C., & Ma, X. (2003). New design approaches to ultra-clean diesel fuels by deep desulfurization and deep dearomatization. *Applied Catalysis B: Environmental*, *41*(1-2), 207-238.
13. Babich, I. V., & Moulijn, J. A. (2003). Science and technology of novel processes for deep desulfurization of oil refinery streams: a review. *Fuel*, *82*(6), 607-631.
14. Kim, J. H., Ma, X., Zhou, A., & Song, C. (2006). Ultra-deep desulfurization and denitrogenation of diesel fuel by selective adsorption over three different adsorbents: a study on adsorptive selectivity and mechanism. *Catalysis Today*, *111*(1-2), 74-83.
15. Anastas, P., & Eghbali, N. (2010). Green chemistry: principles and practice. *Chemical Society Reviews*, *39*(1), 301-312.

16. Huddleston, J. G., Visser, A. E., Reichert, W. M., Willauer, H. D., Broker, G. A., & Rogers, R. D. (2001). Characterization and comparison of hydrophilic and hydrophobic room temperature ionic liquids incorporating the imidazolium cation. *Green chemistry*, *3*(4), 156-164.
17. Brennecke, J. F., & Maginn, E. J. (2001). Ionic liquids: innovative fluids for chemical processing. *AIChE Journal*, *47*(11), 2384-2389.
18. Garcia, C. L., & Lercher, J. A. (1992). Adsorption and surface reactions of thiophene on ZSM 5 zeolites. *The Journal of Physical Chemistry*, *96*(6), 2669-2675.
19. Richardeau, D., Joly, G., Canaff, C., Magnoux, P., Guisnet, M., Thomas, M., & Nicolaos, A. (2004). Adsorption and reaction over HFAU zeolites of thiophene in liquid hydrocarbon solutions. *Applied Catalysis A: General*, *263*(1), 49-61.
20. Chica, A., Strohmaier, K. G., & Iglesia, E. (2005). Effects of zeolite structure and aluminum content on thiophene adsorption, desorption, and surface reactions. *Applied Catalysis B: Environmental*, *60*(3-4), 223-232.
21. Takahashi, A., Yang, F. H., & Yang, R. T. (2002). New sorbents for desulfurization by π-complexation: thiophene/benzene adsorption. *Industrial & Engineering Chemistry Research*, *41*(10), 2487-2496.
22. Xue, M., Chitrakar, R., Sakane, K., Hirotsu, T., Ooi, K., Yoshimura, Y., ... & Sumida, N. (2005). Selective adsorption of thiophene and 1-benzothiophene on metal-ion-exchanged zeolites in organic medium. *Journal of colloid and interface science*, *285*(2), 487-49.
23. Tetrahydrothiophene, T. (2003). Mechanistic investigations on the adsorption of organic sulfur compounds over solid adsorbents in the adsorptive desulfurization of transportation fuels. *Prepr. Pap.-Am. Chem. Soc., Div. Fuel Chem*, *48*(2), 693.
24. Velu, S., Ma, X., & Song, C. (2002). Zeolite-based adsorbents for desulfurization of jet fuel by selective adsorption. *Fuel Chemistry Division Preprints*, *47*(2), 447-448.
25. Bhandari, V. M., Ko, C. H., Park, J. G., Han, S. S., Cho, S. H., & Kim, J. N. (2006). Desulfurization of diesel using ion-exchanged zeolites. *Chemical Engineering Science*, *61*(8), 2599-2608.
26. Yang, R. T., Hernández-Maldonado, A. J., & Yang, F. H. (2003). Desulfurization of transportation fuels with zeolites under ambient conditions. *Science*, *301*(5629), 79-81.
27. Hernández-Maldonado, A. J., Yang, F. H., Qi, G., & Yang, R. T. (2005). Desulfurization of transportation fuels by π-complexation sorbents: Cu (I)-, Ni (II)-, and Zn (II)-zeolites. *Applied Catalysis B: Environmental*, *56*(1-2), 111-126.
28. Jian-long, W. A. N. G., Zhao, D. S., Zhou, E. P., & Zhi, D. O. N. G. (2007). Desulfurization of gasoline by extraction with N-alkyl-pyridinium-based ionic liquids. *Journal of fuel chemistry and technology*, *35*(3), 293-296.
29. Yang, R. T. (2003). *Adsorbents: fundamentals and applications*. John Wiley & Sons.
30. Spoto, G., Geobaldo, F., Bordiga, S., Lamberti, C., Scarano, D., & Zecchina, A. (1999). Heterocycles oligomerization in acidic zeolites: a UV-visible and IR study. Topics in Catalysis, 8(3-4), 279.

31. 31. https://iupac.org/
32. Gillett, S. L. (1997, November). Toward a Silicate-Based Molecular Nanotechnology I. Background and Review. In *The Fifth Foresight Conference on Molecular Nanotechnology, Palo Alto California.*
33. http://www.iza-online.org/
34. M. K. Rubin, "Composition of synthetic porous crystalline material, its synthesis and use," U .S. Patent, 49454325, 1990.
35. Leonowicz, M. E., Lawton, J. A., Lawton, S. L., & Rubin, M. K. (1994). MCM-22: a molecular sieve with two independent multidimensional channel systems. *science*, *264*(5167), 1910-1913.
36. A. Corma, V. Fornés, S. B. C. Pergher, Th. L. Maesen and J. G. Buglass, Nature, 1998, 396, 353–356
37. Margarit, V. J., Martínez‐Armero, M. E., Navarro, M. T., Martínez, C., & Corma, A. (2015). Direct Dual‐Template Synthesis of MWW Zeolite Monolayers. *Angewandte Chemie International Edition*, *54*(46), 13724-13728.
38. Weitkamp, J. (2000). Zeolites and catalysis. *Solid State Ionics*, *131*(1-2), 175-188.
39. Hernández-Maldonado, A. J., Yang, F. H., Qi, G., & Yang, R. T. (2005). Desulfurization of transportation fuels by π-complexation sorbents: Cu (I)-, Ni (II)-, and Zn (II)-zeolites. *Applied Catalysis B: Environmental*, *56*(1-2), 111-126.
40. Inayat, A., Knoke, I., Spiecker, E., & Schwieger, W. (2012). Assemblies of mesoporous FAU‐type zeolite nanosheets. *Angewandte Chemie International Edition*, *51*(8), 1962-1965.
41. Olson, D. H., Kokotailo, G. T., Lawton, S. L., & Meier, W. M. (1981). Crystal structure and structure-related properties of ZSM-5. *The Journal of Physical Chemistry*, *85*(15), 2238-2243.
42. Choi, M., Na, K., Kim, J., Sakamoto, Y., Terasaki, O., & Ryoo, R. (2009). Stable single-unit-cell nanosheets of zeolite MFI as active and long-lived catalysts. *Nature*, *461*(7261), 246.
43. Khaleel, M., Wagner, A. J., Mkhoyan, K. A., & Tsapatsis, M. (2014). On the rotational intergrowth of hierarchical FAU/EMT zeolites. *Angewandte Chemie International Edition*, *53*(36), 9456-9461.
44. Qiao, M. H., Cao, Y., Tao, F., Liu, Q., Deng, J. F., & Xu, G. Q. (2000). Electronic and vibrational properties of thiophene on Si (100). *The Journal of Physical Chemistry B*, *104*(47), 11211-11219.
45. Mishra, R., Jha, K. K., Kumar, S., & Tomer, I. (2011). Synthesis, properties and biological activity of thiophene: A review. *Der Pharma Chemica*, *3*(4), 38-54.
46. Yong, C., & Renyuan, Q. (1985). IR and Raman studies of polythiophene prepared by electrochemical polymerization. *Solid state communications*, *54*(3), 211-213.
47. Tarbell, D. S. (1954). Compounds with Condensed Thiophene Rings. *Journal of the American Chemical Society*, *76*(22), 5896-5896.
48. Shimizu, K. I., Shibata, J., Yoshida, H., Satsuma, A., & Hattori, T. (2001). Silver-alumina catalysts for selective reduction of NO by higher hydrocarbons: structure of active sites and reaction mechanism. *Applied Catalysis B: Environmental*, *30*(1-2), 151-162.

49. Wang, Z. M., Yamaguchi, M., Goto, I., & Kumagai, M. (2000). Characterization of Ag/Al 2 O 3 de-NO x catalysts by probing surface acidity and basicity of the supporting substrate. *Physical Chemistry Chemical Physics*, *2*(13), 3007-3015.
50. Bogdanchikova, N., Meunier, F. C., Avalos-Borja, M., Breen, J. P., & Pestryakov, A. (2002). On the nature of the silver phases of Ag/Al2O3 catalysts for reactions involving nitric oxide. *Applied Catalysis B: Environmental*, *36*(4), 287-297.
51. Paul, K. K., Ghosh, R., & Giri, P. K. (2016). Mechanism of strong visible light photocatalysis by Ag2O-nanoparticle-decorated monoclinic TiO2 (B) porous nanorods. *Nanotechnology*, *27*(31), 315703.
52. Spoto, G., Geobaldo, F., Bordiga, S., Lamberti, C., Scarano, D., & Zecchina, A. (1999). Heterocycles oligomerization in acidic zeolites: a UV-visible and IR study. *Topics in Catalysis*, *8*(3-4), 279.
53. Geobaldo, F., Palomino, G. T., Bordiga, S., Zecchina, A., & Arean, C. O. (1999). Spectroscopic study in the UV-Vis, near and mid IR of cationic species formed by interaction of thiophene, dithiophene and terthiophene with the zeolite HY. *Physical Chemistry Chemical Physics*, *1*(4), 561-569.
54. Bein, T., & Enzel, P. (1989). Encapsulation of polypyrrole chains in zeolite channels. *Angewandte Chemie International Edition in English*, *28*(12), 1692-1694.
55. Enzel, P., & Bein, T. (1989). Intrazeolite synthesis of polythiophene chains. *Journal of the Chemical Society, Chemical Communications*, (18), 1326-1327.
56. Geobaldo, F., Spoto, G., Bordiga, S., Lamberti, C., & Zecchina, A. (1997). Propene oligomerization on H-mordenite: Hydrogen-bonding interaction, chain initiation, propagation and hydrogen transfer studied by temperature-programmed FTIR and UV–VIS spectroscopies. *Journal of the Chemical Society, Faraday Transactions*, *93*(6), 1243-1249.
57. Martin, R. E., & Diederich, F. (1999). Lineare monodisperse π‐konjugierte Oligomere: mehr als nur Modellverbindungen für Polymere. *Angewandte Chemie*, *111*(10), 1440-1469.
58Jacobs, P. A., & Leuven, K. U. (1982). Acid zeolites: An attempt to develop unifying concepts (PH Emmett award address, 1981). *Catalysis Reviews Science and Engineering*, *24*(3), 415-440.
59. Katada, N., Suzuki, K., Noda, T., Sastre, G., & Niwa, M. (2009). Correlation between Brønsted acid strength and local structure in zeolites. *The Journal of Physical Chemistry C*, *113*(44), 19208-19217.
60. Datka, J., Boczar, M., & Rymarowicz, P. (1988). Heterogeneity of OH groups in NaH ZSM-5 zeolite studied by infrared spectroscopy. *Journal of Catalysis*, *114*(2), 368-376.
61. Zeng, Y., Moghadam, P. Z., & Snurr, R. Q. (2015). Pore size dependence of adsorption and separation of thiophene/benzene mixtures in zeolites. *The Journal of Physical Chemistry C*, *119*(27), 15263-15273.